PART III

Q^2PSK Modulation and Coding: PERFORMANCE EVALUATION

CHAPTER 7

PERFORMANCE EVALUATION

This chapter presents the performance results of the Q²PSK and Constant Envelope Q²PSK modems in the presence of impairments due to AWGN, ISI from bandlimiting and fading, due to the mobile V/UHF radio communication environment. The integration and evaluation of the developed carrier tracking strategies are carried out. The validity and efficiency of the said algorithms are evaluated under typical mobile channel conditions. Furthermore, the bit error probability graphs are presented to compare the performance of the classical, trellis and multiple trellis codes designed in Part II of this study. The derived upper bounds on bit error probability are benchmarked under typical channel conditions based on the same criteria of equal complexity and throughput.

7.1 INTRODUCTION

The performance evaluations are started by investigation of the uncoded Q²PSK and constant envelope CE-Q²PSK by appropriate modem back-to-back tests in AWGN, followed by evaluations in the presence of phase and frequency uncertainties. Then the evaluation of the convolutional (Classic, TCM and MTCM) trellis codes under similar AWGN channel conditions will be carried out. The second half of this chapter deals with the performance evaluation of the uncoded and coded Q²PSK and CE-Q²PSK modem under mobile fading channel conditions.

7.1.1 SNR versus E_b/N_o

Before the performance investigation is continued, probably the most important quantity in the evaluation of different communications systems, namely the required SNR measured in dB, is quantified. Conventional power requirements are concerned with the average carrier power C, and

the average noise power N. The ratio C/N, is however meaningless unless the noise bandwidth of the receiver is specified. For this reason it is necessary to normalise the ratio C/N so that it becomes independent of bandwidth. The result of this normalisation is the quantity E_b/N_o, which becomes the independent variable in all subsequent BER measurements.

By specifying the required E_b/N_o in dB, the correct scale factor is calculated by which the noise samples are weighted to produce the required noise variance σ_r^2 [58, 82]. The noise is added to the output of the Q^{2}PSK transmitter to produce the required E_b/N_o ratio. By introducing the signal bandwidth, W (taken to be 10.0 kHz in this study) the following relationship between SNR and E_b/N_o can be written for binary signals,

$$\begin{aligned} \text{SNR} \doteq P_s/P_n &= \frac{\sigma_s^2}{\sigma_r^2}, \quad \text{(In the bandwidth W of the signal)} \\ &= \frac{E_b R_b}{N_o W} \end{aligned} \tag{7.1}$$

where

$$\begin{aligned} \sigma_s^2 &= \text{signal variance} \\ \sigma_r^2 &= \text{required noise variance} \\ E_b &= \text{nominal energy per bit} \\ R_b &= 1/T_b = \text{nominal bit rate} \\ N_o &= \text{Level of single-sided power spectral density of white noise} \end{aligned} \tag{7.2}$$

Equation (7.1) can be manipulated to obtain an expression for the required noise variance to obtain a specified E_b/N_o ratio. This produces

$$\sigma_r^2 = \frac{\sigma_s^2 \cdot W}{10^{\left(\frac{E_b}{N_o}\frac{1}{10}\right)} \cdot R_b} \tag{7.3}$$

where E_b/N_o has been specified in dB.

The noise generator used in the simulation is based on the Wichmann-Hill algorithm (see Byte, 1984), and employs the Marsaglia-Bray transformation to generate AWGN with variance $\sigma_n^2 = N_n f_{samp}/2 = 1$ $Watt$, where f_{samp} is the sampling frequency. From this expression, N_n can be obtained

$$N_n = \frac{2}{f_{samp}} \tag{7.4}$$

Both σ_n^2 and N_n will have to be weighted with a constant k_r, to obtain the required noise variance σ_r^2 for a specified E_b/N_o ratio. This constant is obtained as follows:

$$k_r = \frac{\sigma_r^2}{\sigma_n^2} = \sigma_r^2, \quad \text{since } \sigma_n^2 = 1 \tag{7.5}$$

producing

$$k_r = \frac{\sigma_s^2 \cdot f_{samp}}{10^{\left(\frac{E_b}{N_o}\frac{1}{10}\right)} \cdot 2R_b} \tag{7.6}$$

The noise samples must finally be weighted by the square root of k_r, since k_r is a power scale factor, and noise samples are generated in *volt*. Since the Marsaglia-Bray algorithm produces noise samples with unit variance, $\sigma_n^2 = 1$ $Watt$, scaling by $\sqrt{k}$ will directly produce noise samples with variance σ_r^2, as required by (7.1) [82].

7.1.2 Simulation software

Detail concerning the implementation of the Q²PSK mobile communication system in software (written in *C* and *C++*), can be found in technical research reports of the Laboratory for Advanced Engineering at the University of Pretoria [83, 84, 85, 86, 87, 88]. Complete descriptions of the software developed over a long period of time, as well as the actual simulation software utilised in this study, are contained in these reports.

7.2 EVALUATION ON AWGN CHANNELS

The AWGN, or static (non-fading) channel is probably the most studied channel in communication system evaluation. In this section the modem's performance under these static channel conditions will be investigated.

Block diagrams of the digital Q²PSK modulator and demodulator were given and analysed in detail in Chapter 4. At the receiver the blocks labeled 'BPF', i.e., the bandpass filters, were implemented by modulating specific lowpass filter responses to the desired passband frequencies. For all the simulation results presented in this chapter the lowpass impulse responses were taken to be full Nyquist LPFs with roll-off factors of $\alpha = 0.5$. The Intermediate Frequency (IF) is chosen as 12.5 *kHz*.

The geometry of the Q²PSK hypercube is affected by bandlimiting since the orthogonality of the data shaping pulses, $q_1(t)$ and $q_2(t)$ may be partially lost in the process. The loss of orthogonality causes ISI, resulting in loss of system performance (i.e., a degradation of BER performance).

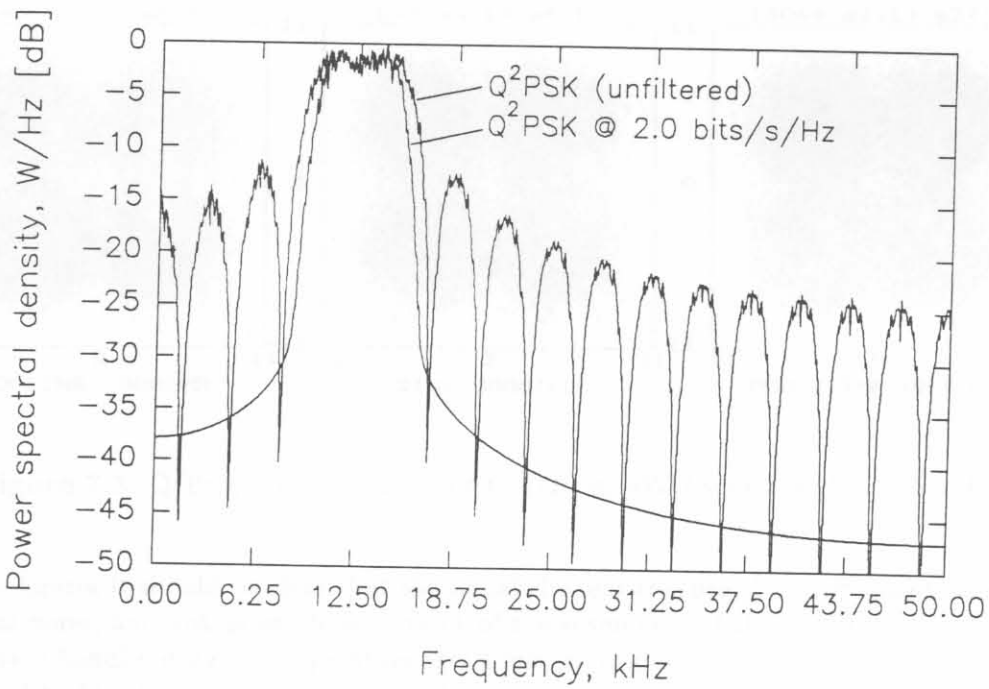

Figure 7.1: Power spectral densities of unfiltered and filtered Q²PSK (CE-Q²PSK).

Figure 7.1 shows the power spectral densities of unfiltered and filtered Q^{2}PSK (CE-Q^{2}PSK). The latter modem has an effective bandwidth efficiency, $\eta_f = 2.0$ *bits/s/Hz*. It was shown by Saha [12] that under these bandlimiting conditions the effect of ISI interference on the Q^{2}PSK signal is as mild as the effects of ISI on QPSK when operating at 1.0 *bit/s/Hz*.

An effective way of displaying the qualitative effects of ISI is to construct the signal space constellations in accordance with the discussion in Chapter 4 (see Figure 4.7). Figures 7.2 to 7.3 depict the bandlimited Q^{2}PSK signal constellations operating at 2.0 *bits/s/Hz* in AWGN with $E_b/N_o = 25.0$ and 5.0 *dB*, respectively.

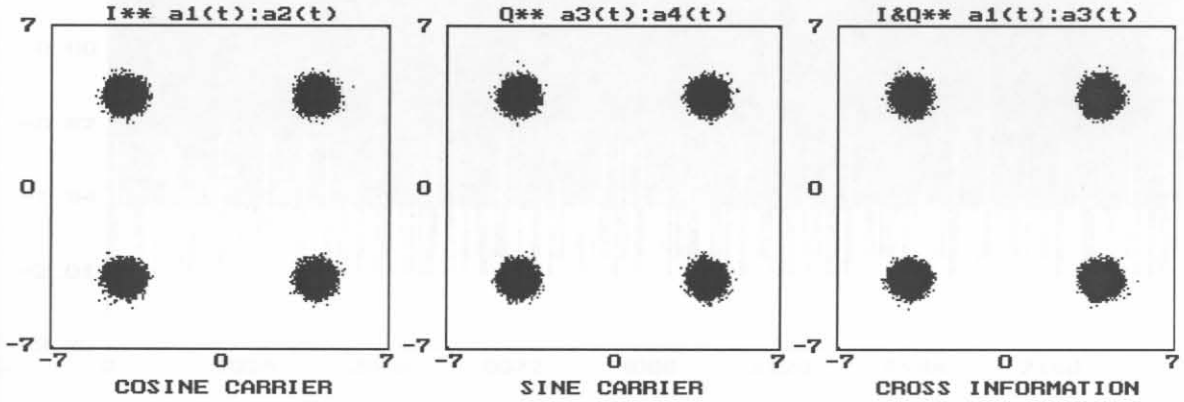

Figure 7.2: Q^{2}PSK operating at 2.0 *bits/s/Hz* in AWGN with $E_b/N_o = 25.0$ *dB*.

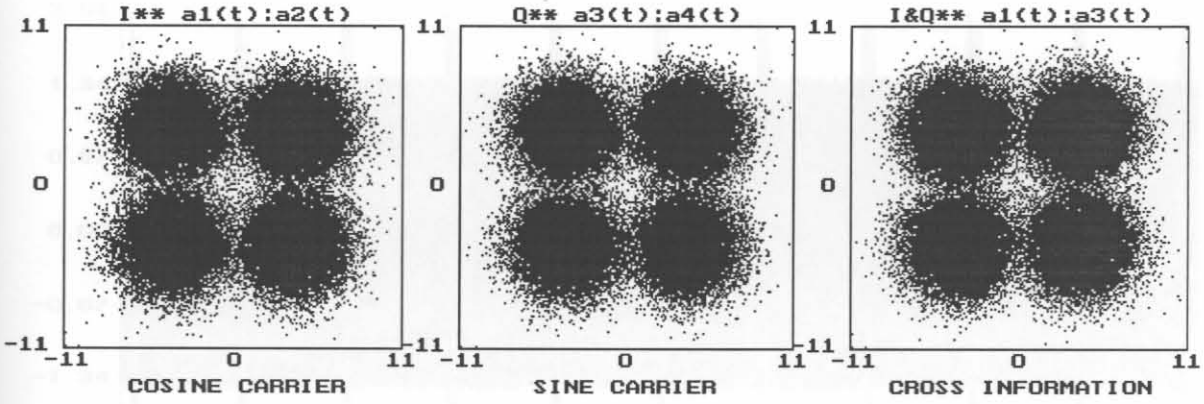

Figure 7.3: Q^{2}PSK operating at 2.0 *bits/s/Hz* in AWGN with $E_b/N_o = 5.0$ *dB*.

From these figures it should be clear that the signal clusters are spread out primarily as a result of the thermal noise, and not as much as a result of the severeness of the bandlimiting. In the case of more severe bandlimiting (i.e., operation at 2.4 *bits/s/Hz* and higher) the ISI is more severe and clusters tend to blend into neighboring signal points, as is to be expected These figures show the correct phase positions, in the absence of any carrier phase or frequency offset. The former error will manifest itself as a constant phase offset of θ_0 *rad*, whereas the latter will result in a constant rotation of the phase symbols at a rate equal to the frequency difference between the local carrier

in-phase I and quadrature phase Q references, and the received Q^{2}PSK signal. These above results will serve as reference for the simulation tests to follow.

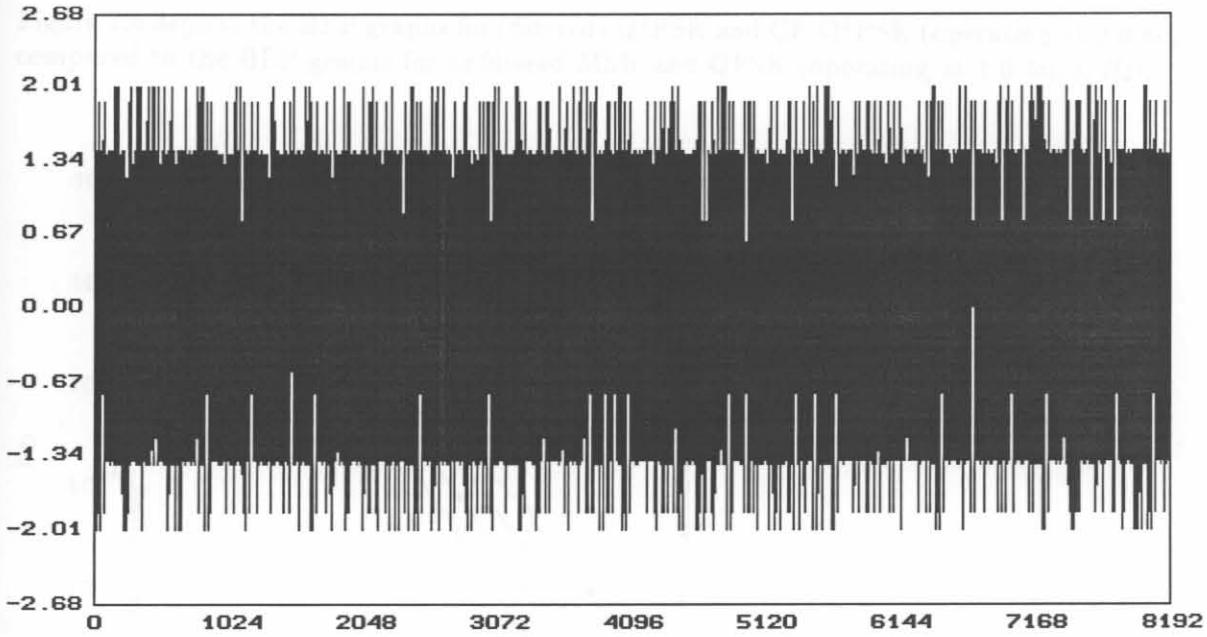

Figure 7.4: Q^{2}PSK signal under static channel conditions (X-axis: samples, Y-axis: volt).

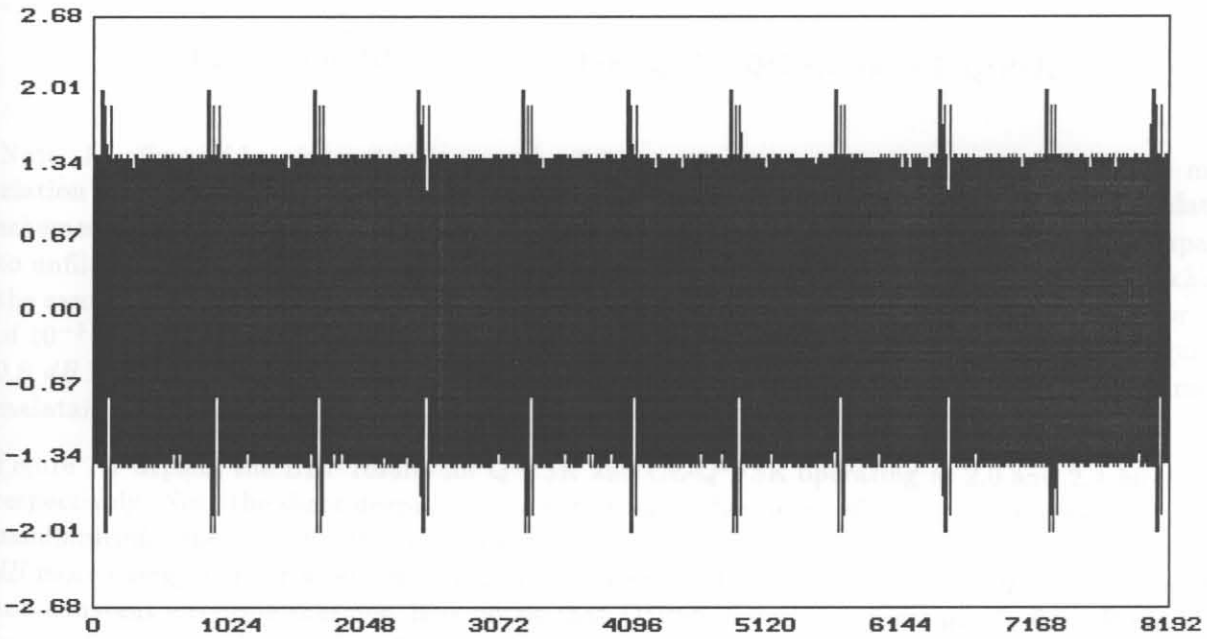

Figure 7.5: CE-Q^{2}PSK signal under static channel conditions.

Figures 7.4 and 7.5 depict the discrete time (sampled) signals for Q^{2}PSK and CE-Q^{2}PSK transmitted over the bandlimited AWGN channel, for a SNR of $E_b//N_o = 35$ dB. Note the non-constant envelope of the Q^{2}PSK signal, whereas the CE-Q^{2}PSK signal envelope is constant except over the

(8 or 16 symbol) header (designed for optimum correlation properties), preceding each data frame according to the block transmission strategy outlined in section 4.2, Figure 4.11.

Figure 7.6 depicts the BEP graphs for (filtered) Q²PSK and CE-Q²PSK (operating at 2.0 *bits/s/Hz*) compared to the BEP graphs for unfiltered MSK and QPSK (operating at 1.0 *bit/s/Hz*).

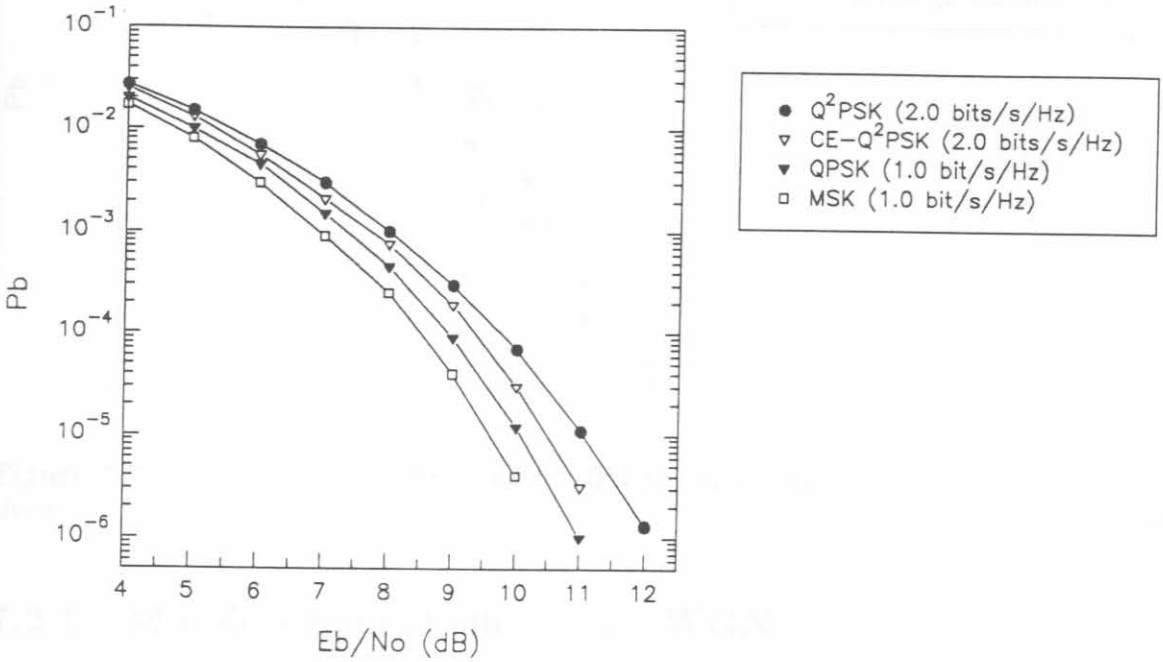

Figure 7.6: BEP curves for MSK, QPSK, Q²PSK, and CE-Q²PSK.

Note the effect of bandpass filtering on the BEP performance curves of the forementioned modulation schemes. Recall from the analysis carried out in Chapter 2 that all of the modulation schemes shown have exactly the same theoretical BEP. From Figure 7.6 it is noted that compared to unfiltered MSK and QPSK, Q²PSK requires, respectively 1.5 and 1.1 *dB* more energy to achieve the same error performance at $P_b = 10^{-5}$. Furthermore, Q²PSK requires to achieve a bit error rate of 10^{-5}, an E_b/N_o of 11.1 *dB*, whereas CE-Q²PSK requires only 10.4 *dB*. This performance gain of 0.6 *dB* is a direct result of the inherent coding gain brought about by the block coding scheme to maintain a constant envelope signal.

Figure 7.7 depicts the BEP results for Q²PSK and CE-Q²PSK operating at 2.0 and 2.4 *bits/s/Hz*, respectively. Note the slight degradation in performance due to the effects of ISI as a result of severe bandlimiting. Specifically, Q²PSK operating at 2.0 *bits/s/Hz* requires 11.1 *dB*, while it requires 1.1 *dB* more energy per bit when operating at a bandwidth-efficiency of 2.4 *bits/s/Hz*. Comparing the non-constant envelope schemes, it is noted that Q²PSK requires approximately 0.9 *dB* more bit energy to achieve the same performance when operating at 2.4 *bits/s/Hz*, compared to operating at 2.0 *bits/s/Hz*.

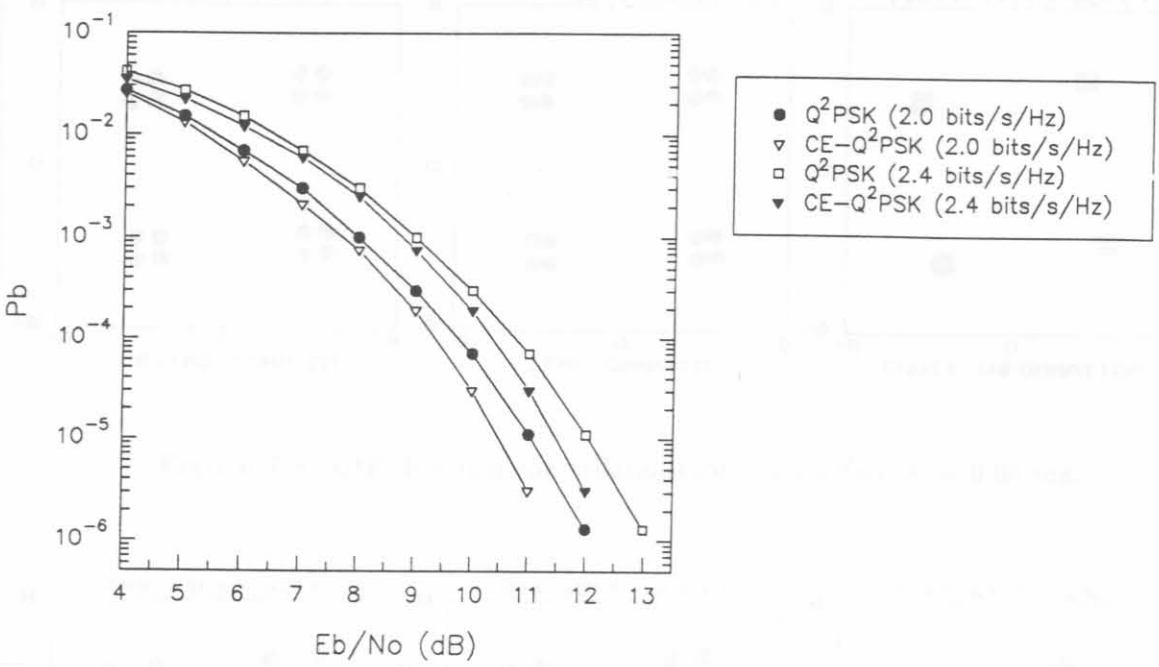

Figure 7.7: BEP curves for Q²PSK and CE-Q²PSK, operating at 2.0 and 2.4 *bits/s/Hz*, respectively.

7.2.1 Mobile Channel effects in AWGN

In this section the effects of mobile channel non-linearities will be investigated on the performance of the Q²PSK modem. The BEP performance curves are shown for values of phase and Doppler frequency normalised by the symbol rate, $R_s = 1/T_s$. The normalised phase offsets $\theta_o T_s$ range from 10×10^{-6} to 40×10^{-6} at a bit rate of $R_b = 20.0$ *kbits/s*, this range corresponds to phase offsets in the range 0.05 to 0.2 *rad*.

For vehicle speeds of 30, 60 and 120 *km/h*, and a carrier frequency of 900 *MHz*, the corresponding Doppler frequencies are 25, 50 and 100 *Hz*, respectively. For these vehicle speeds and bit rate, the normalised Doppler frequency, $f_D T_s$, ranges from 5×10^{-3} to 20×10^{-3}. In satellite mobile systems however, much higher Doppler frequencies will be experienced.

Figures 7.8 to 7.10 display the Q²PSK modem signal constellations for phase offsets θ_o of 0.05, 0.1 and 0.2 *rad*, respectively, with $E_b/N_o = 30$ *dB*. The phase offsets result in the signal constellation clusters to be rotated with an amount corresponding to the phase offset. Figures 7.11 to 7.13 display the Q²PSK modem signal constellations for Doppler frequencies, f_D of 25, 50 and 100 *Hz* and $E_b/N_o = 30$ *dB*. The Doppler frequencies result in a constant rotation of the phase symbols at a rate equal to the frequency difference between the local carrier references, and the received Q²PSK signal, over one symbol period.

Figures 7.14 to 7.16 illustrates the effects of phase offsets on the CE-Q²PSK signal space constellations for values of θ_o in the above ranges. Interestingly, when these constellations are compared with those presented in Figures 7.8 to 7.10, it is noted that the phase effects are restricted. This can easily be explained. Recall, in order to force a constant envelope signal, a block coder of rate-3/4 is utilised. The effect of this coder is to add an amount of redundancy to one of the four information carrying data streams, resulting in a 1/4 reduction in dimensionality. Therefore, the qualitative

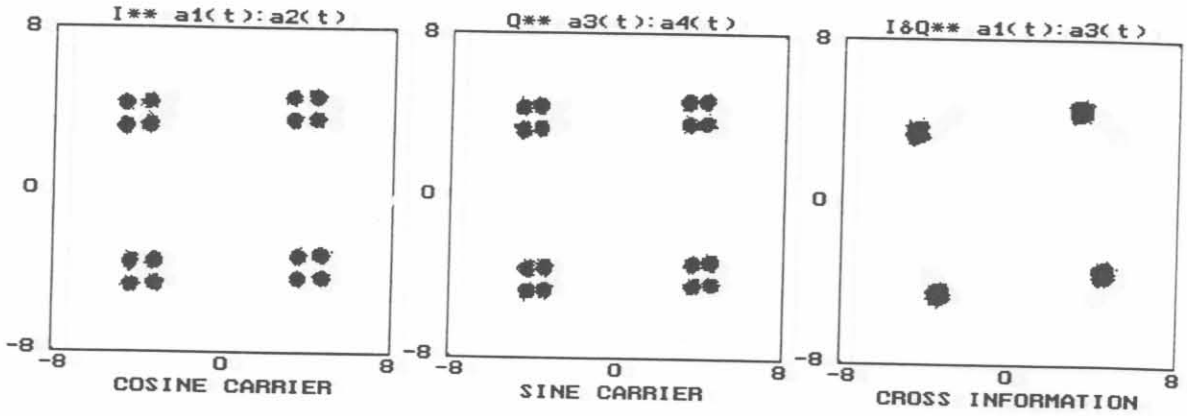

Figure 7.8: Q^2PSK signal constellations for phase offset, $\theta_o = 0.05$ *rad.*

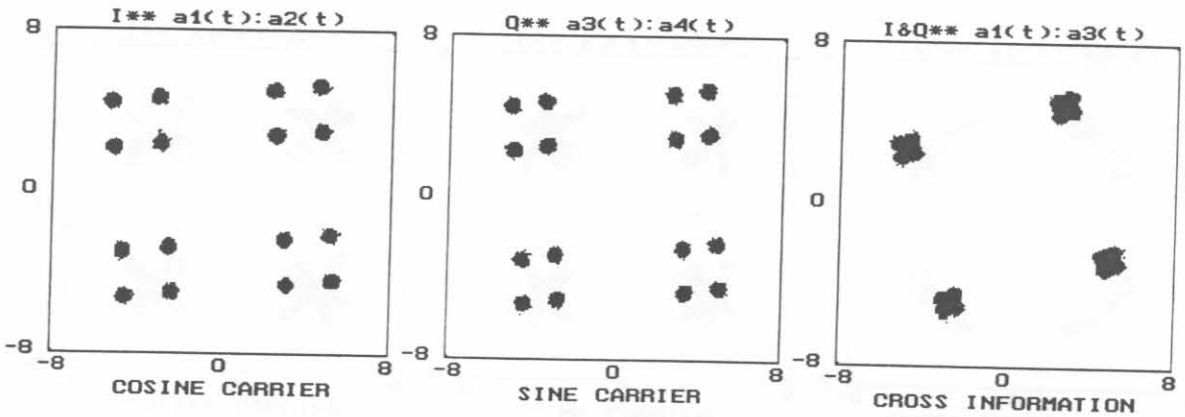

Figure 7.9: Q^2PSK signal constellations for phase offset, $\theta_o = 0.1$ *rad.*

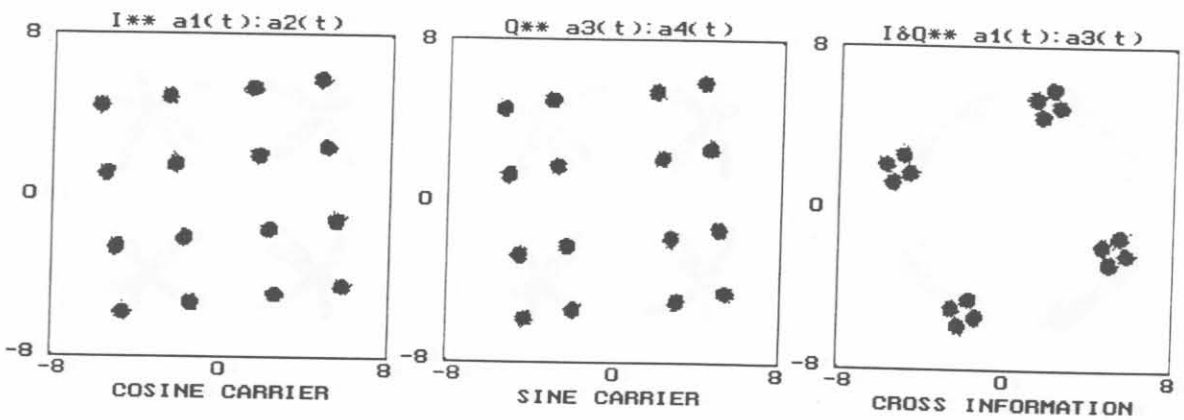

Figure 7.10: Q^2PSK signal constellations for phase offset, $\theta_o = 0.2$ *rad.*

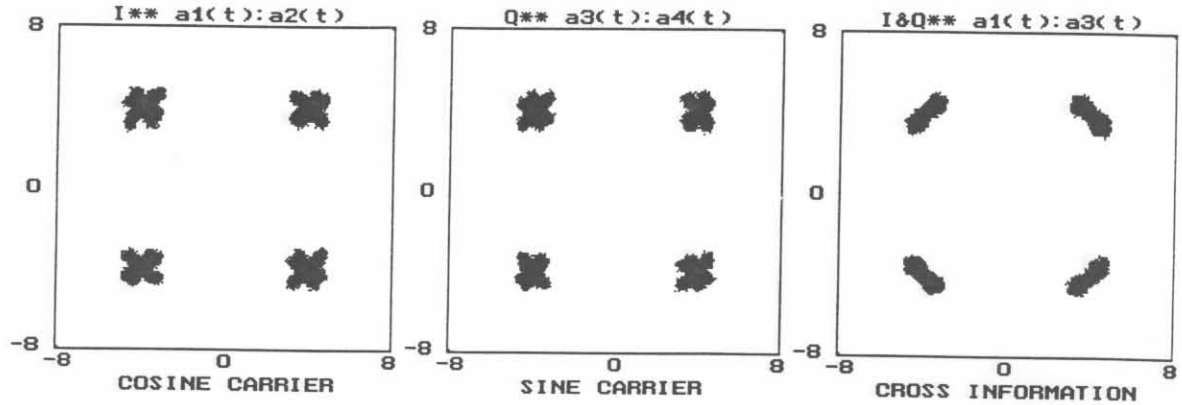

Figure 7.11: Q^2PSK signal constellations for Doppler frequency of 25 *Hz* at RF frequency of 900 *MHz*.

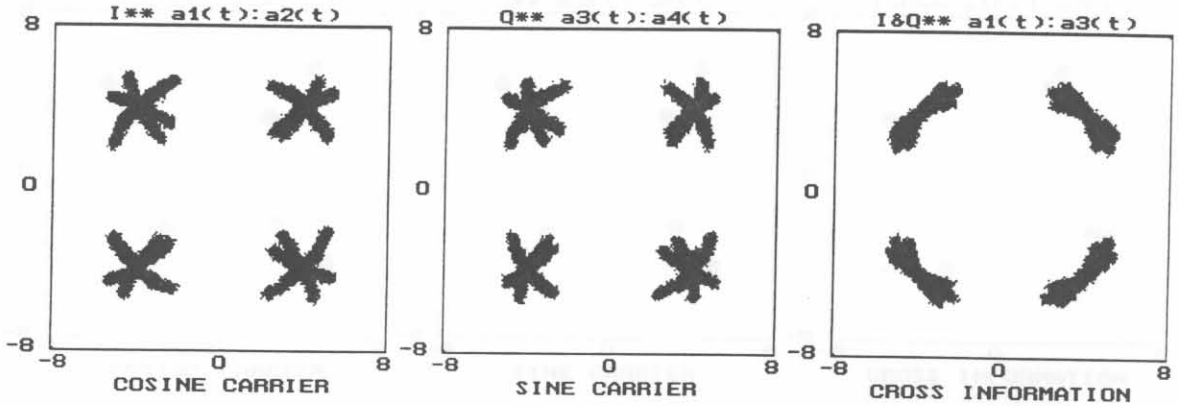

Figure 7.12: Q^2PSK signal constellations for Doppler frequency of 50 *Hz*.

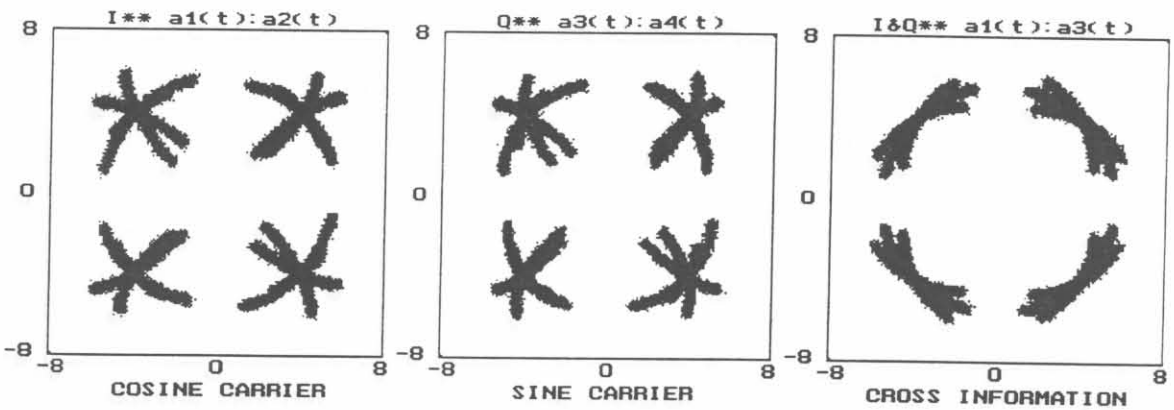

Figure 7.13: Q^2PSK signal constellations for Doppler frequency of 100 *Hz*.

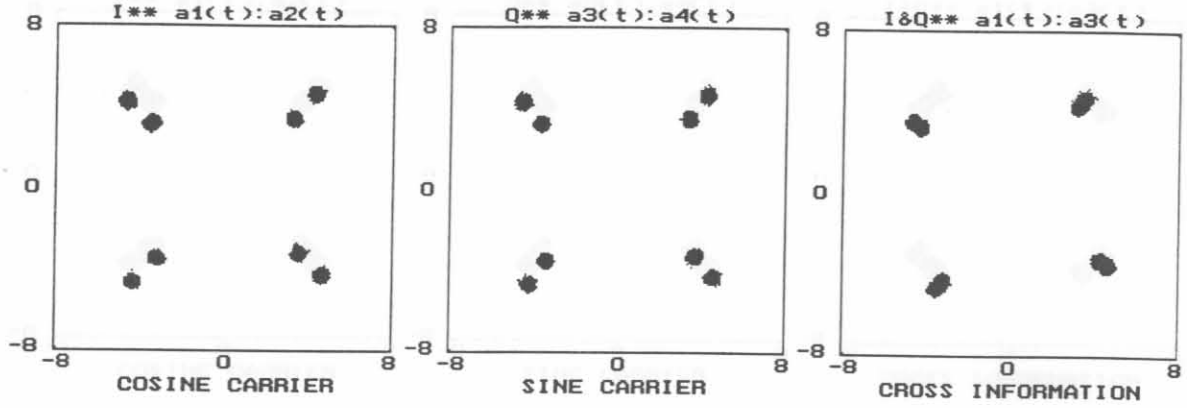

Figure 7.14: CE-Q^{2}PSK signal constellations for phase offset, $\theta_o = 0.01$ *rad.*

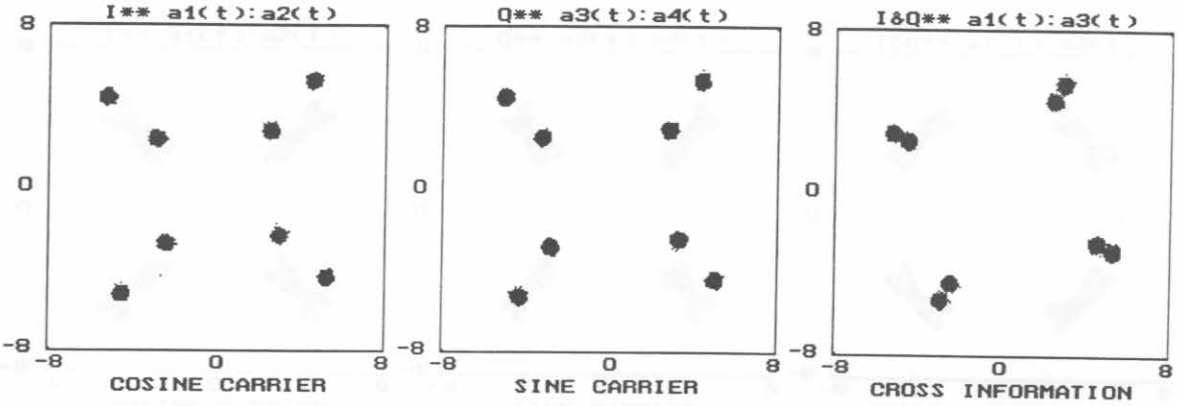

Figure 7.15: CE-Q^{2}PSK signal constellations for phase offset, $\theta_o = 0.1$ *rad.*

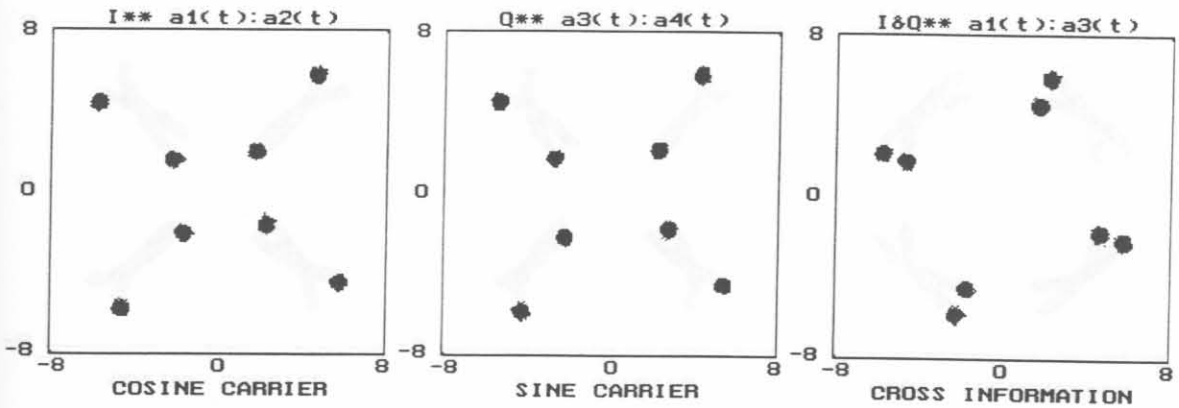

Figure 7.16: CE-Q^{2}PSK signal constellations for phase offset, $\theta_o = 0.2$ *rad.*

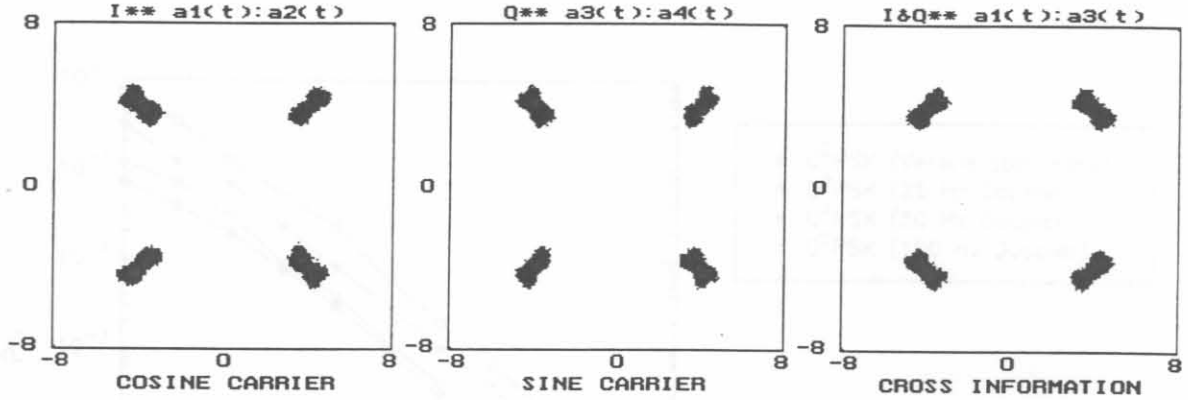

Figure 7.17: CE-Q^{2}PSK signal constellations for Doppler frequency of 25 *Hz* at RF frequency of 900 *MHz*.

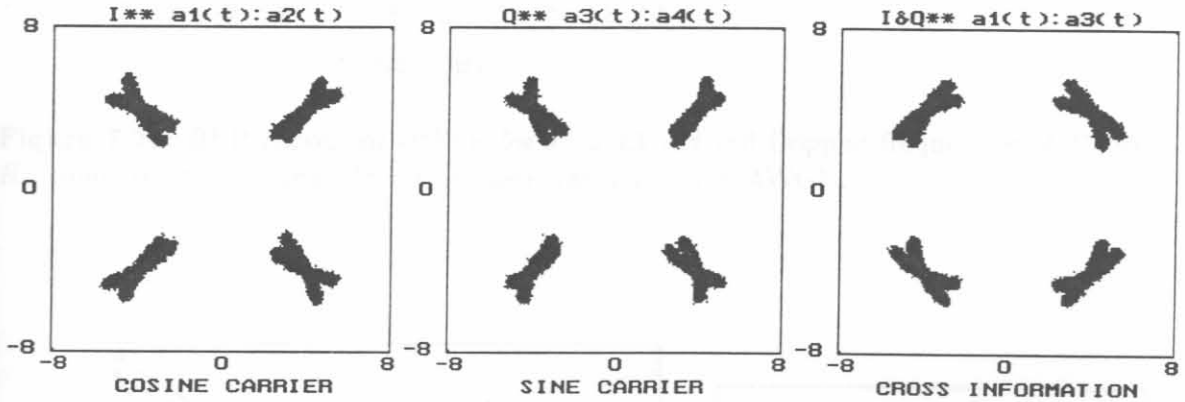

Figure 7.18: CE-Q^{2}PSK signal constellations for Doppler frequency of 50 *Hz*.

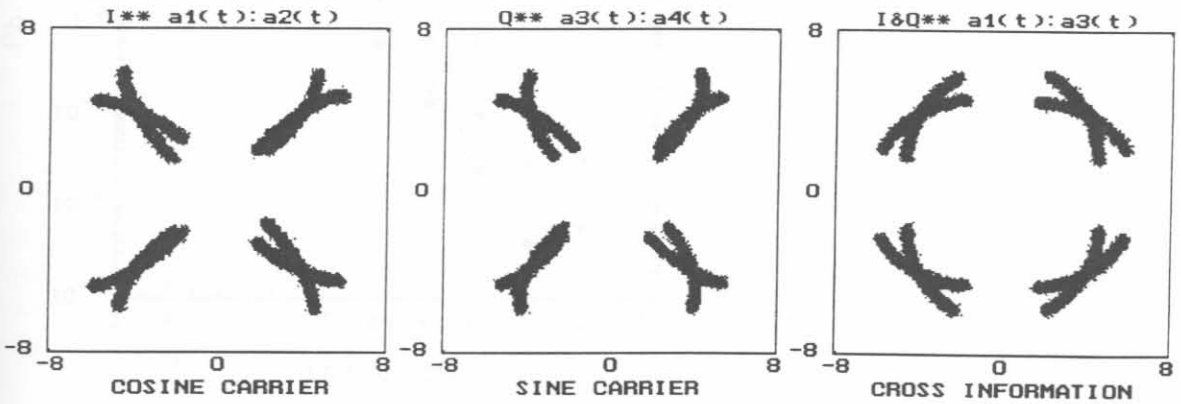

Figure 7.19: CE-Q^{2}PSK signal constellations for Doppler frequency of 100 *Hz*.

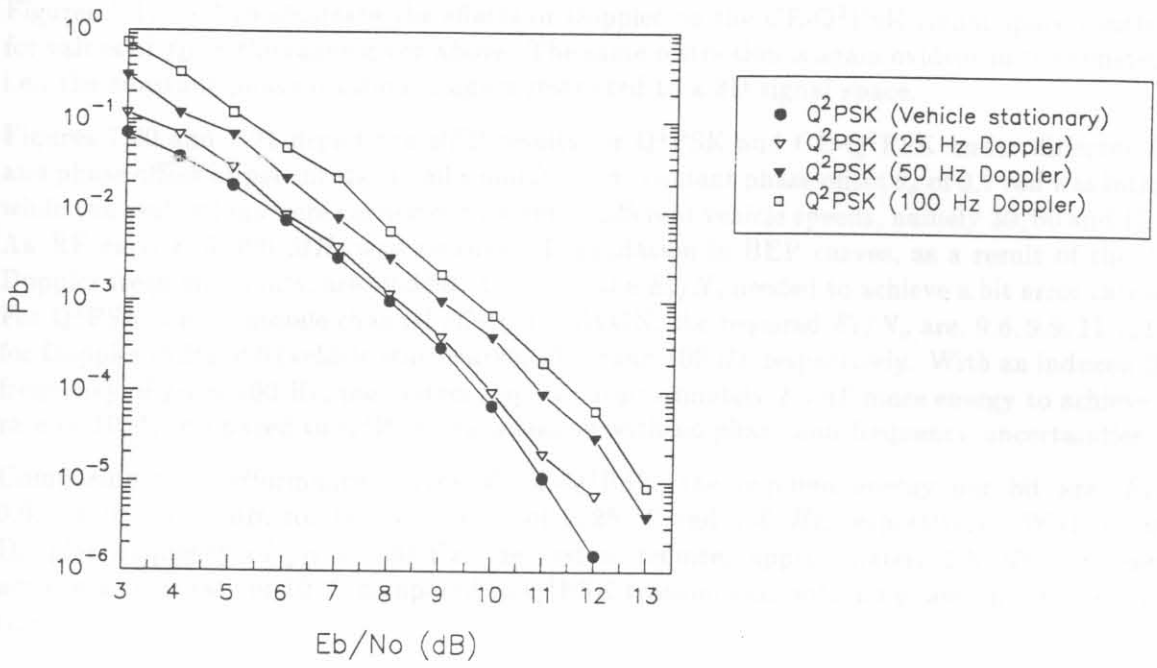

Figure 7.20: BEP curves for Q²PSK for $\theta_o = 0.1$ *rad* and Doppler frequencies of 25, 50 and 100 *Hz*, compared to the ideal Q²PSK modem transmission in AWGN.

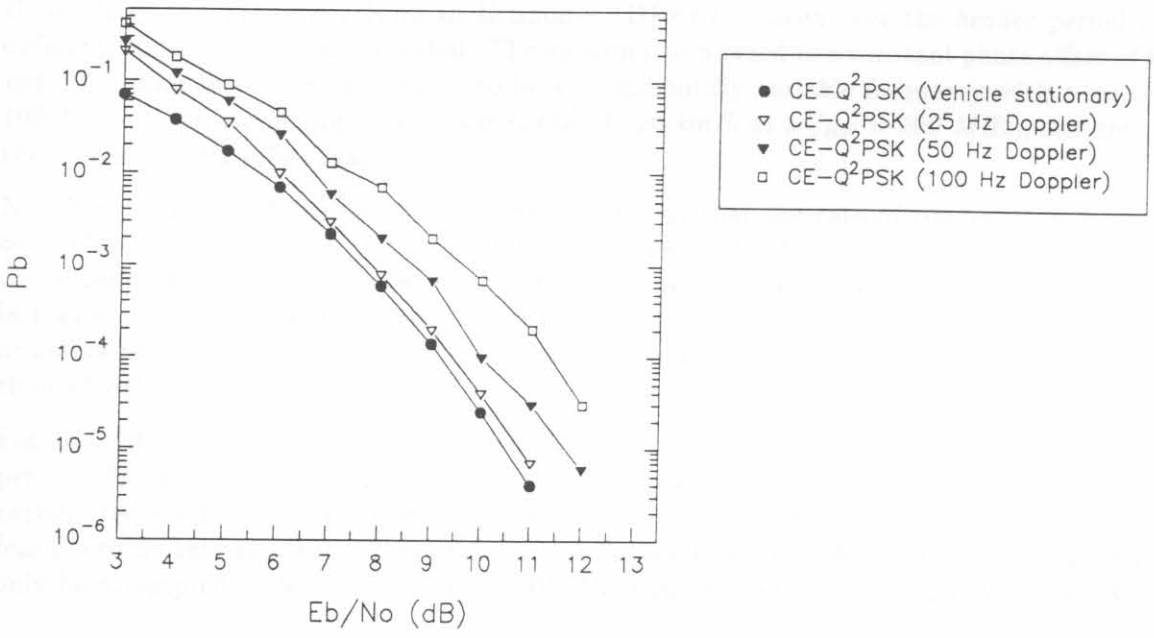

Figure 7.21: BEP curves for CE-Q²PSK for $\theta_o = 0.1$ *rad* and Doppler frequencies of 25, 50 and 100 *Hz*, compared to the ideal CE-Q²PSK modem transmission in AWGN.

effects of phase non-linearities are restricted to a three-dimensional (3D) signal space.

Figures 7.17 to 7.19 illustrate the effects of Doppler on the CE-Q^{2}PSK signal space constellations for values of f_D in the range given above. The same restriction is again evident in the constellations, i.e., the constant phase rotation is again restricted to a 3D signal space.

Figures 7.20 and 7.21 depict the BEP results for Q^{2}PSK and CE-Q^{2}PSK under different Doppler and phase offset impairments. In all simulations a constant phase offset θ_o of 0.1 *rad* was introduced, while the evaluations were carried out for three different vehicle speeds, namely 30, 60 and 120 *km/h*. An RF carrier of 900 *MHz* was assumed. Degradation in BEP curves, as a result of the different Doppler frequency shifts, are evident. Consider the E_b/N_o needed to achieve a bit error rate of 10^{-4}. For Q^{2}PSK, under mobile channel effects in AWGN, the required E_b/N_o are, 9.6, 9.9, 11.1, 12.0 *dB*, for Doppler shifts of 0 (vehicle stationary), 25, 50 and 100 *Hz*, respectively. With an induced Doppler frequency of $f_D = 100$ Hz, the system requires approximately 2.4 *dB* more energy to achieve a error rate of 10^{-4}, compared to Q^{2}PSK transmission with no phase and frequency uncertainties.

Comparing the performance curves of CE-Q^{2}PSK, the required energy per bit are, $E_b/N_o = 9.0, 9.3, 10.5, 11.5$ *dB*, for Doppler shifts of 0, 25, 50 and 100 *Hz*, respectively. With an induced Doppler frequency of $f_D = 100$ Hz, the system requires approximately 2.5 *dB* more energy to achieve a error rate of 10^{-4}, compared to Q^{2}PSK transmission with no phase and frequency uncertainties.

7.2.2 Phase/Frequency Tracking and Correction

Some simulation results are presented to illustrate the capability of the carrier phase and Doppler frequency offset algorithms discussed in section 4.3, under typical mobile channel conditions.

Figure 7.22 depicts mesh plots of the frequency and phase Minimum Square Error (MSE) for the Dual Phase and Frequency Kalman Estimator (DPFKE), taken over the *header* period only, for different values of E_b/N_o as indicated. The modem is subjected to a constant phase offset of $\theta_o = 0.1$ *rad*. The Doppler frequency is taken to be a cosinusoidally variable frequency with a maximum of 100 *Hz* (i.e., corresponding to a vehicle speed of 120 *km/h* at a $f_{RF} = 900$ *MHz*), centered around the nominal (0 Hz offset) value.

Note from Figure 7.22(a) for the frequency MSE, ρ_k, that the rate of convergence at low values of E_b/N_o is not very fast. However, at higher values of E_b/N_o, i.e., $E_b/N_o > 15$ *dB*, the rate of convergence is significantly higher with acceptable results. Considering the phase MSE, ρ_l, depicted in Figure 7.22(b), it is noted that the DPFKE finds it difficult to effectively track any phase offsets at low values of E_b/N_o. Acceptable convergence rates are again achieved for values of E_b/N_o higher than 15 *dB*.

Figure 7.23 depicts the plots for the DPFKE frequency MSE, ρ_k taken over a part of the data period. The line plot clearly indicates, that at high E_b/N_o values, it is useful to track any possible carrier frequency variations over the data interval. Note, however that it does not seem to be feasible to do this at lower values of E_b/N_o. It is therefore concluded that carrier tracking should only be attempted under relatively good AWGN channel conditions (i.e., $E_b/N_o > 14$ dB).

To Track or *Not To* Track

Figure 7.24 depicts the BEP graphs for the Q^{2}PSK and CE-Q^{2}PSK, under mobile channel conditions in AWGN, with the DPFKE activated. Note that the BEP curves are again given for different

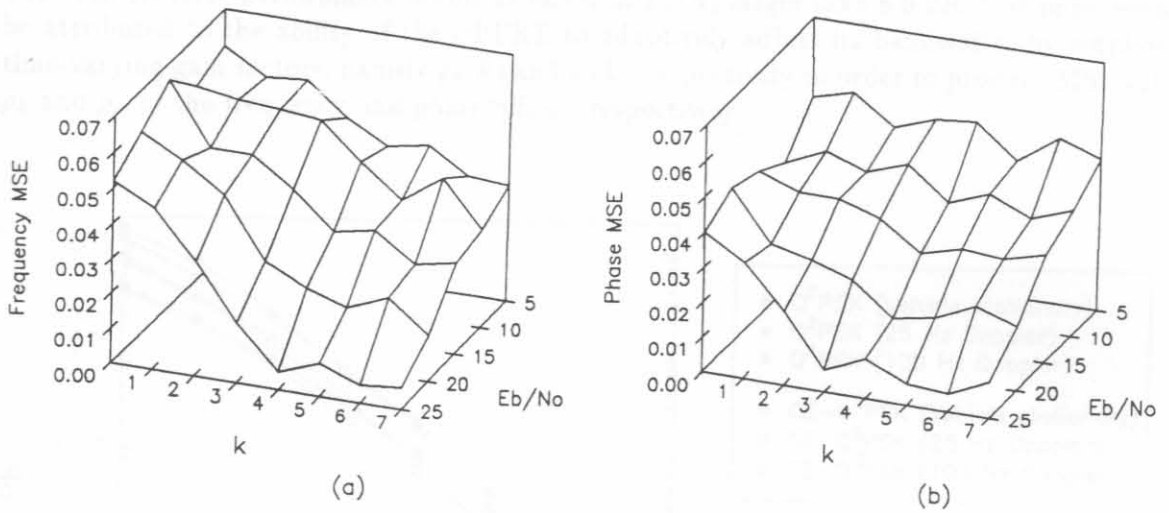

Figure 7.22: Minimum Squared Errors for DPFKE estimator tracking carrier phase and frequency uncertainties over the header period (a) Frequency MSE, ρ_k (b) Phase MSE, ρ_l.

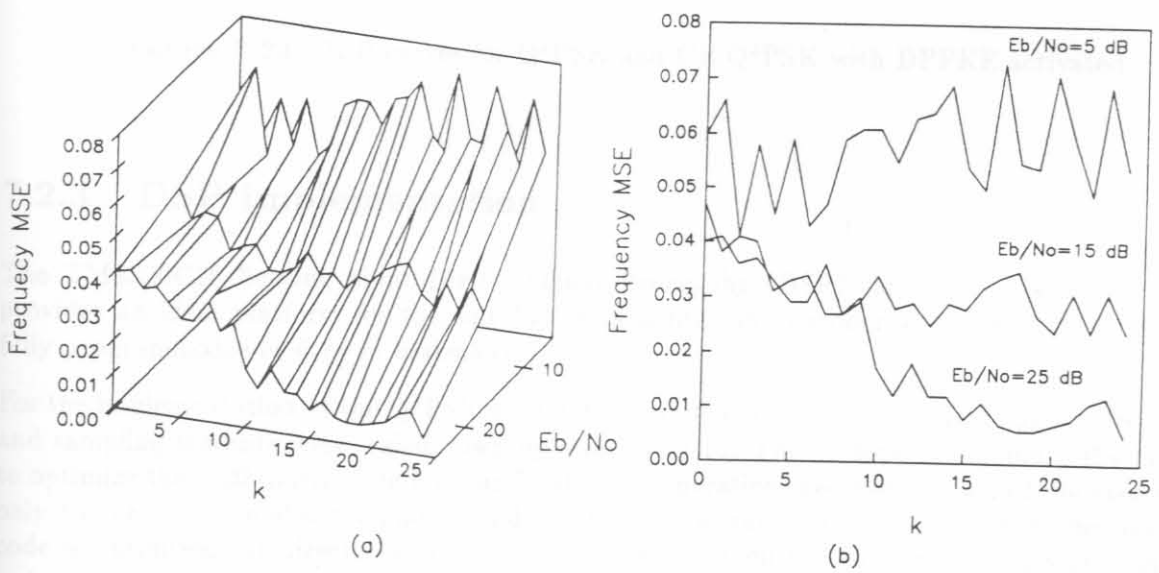

Figure 7.23: Frequency MSE for DPFKE estimator tracking carrier frequency uncertainties over the data period.

Doppler frequency shifts (0, 25, 50 and 100 Hz), and for a constant carrier phase error of $\theta_0 = 0.1$ *rad*. From the BEP curves only a slight degradation in bit error rate performance at low values of E_b/N_o, for frequency shifts up to 100 Hz can be seen. Note also that hardly any noticeable degradation in bit error performance occurs at values of E_b/N_o larger than 8.0 *dB*. This improvement can be attributed to the ability of the DPFKE to adaptively adjust its bandwidth, by employing two time-varying gain factors, namely $\rho_k(k)$ and $\rho_l(k)$, respectively in order to produce MSE estimates, ρ_k and ρ_l, of the frequency and phase offsets, respectively.

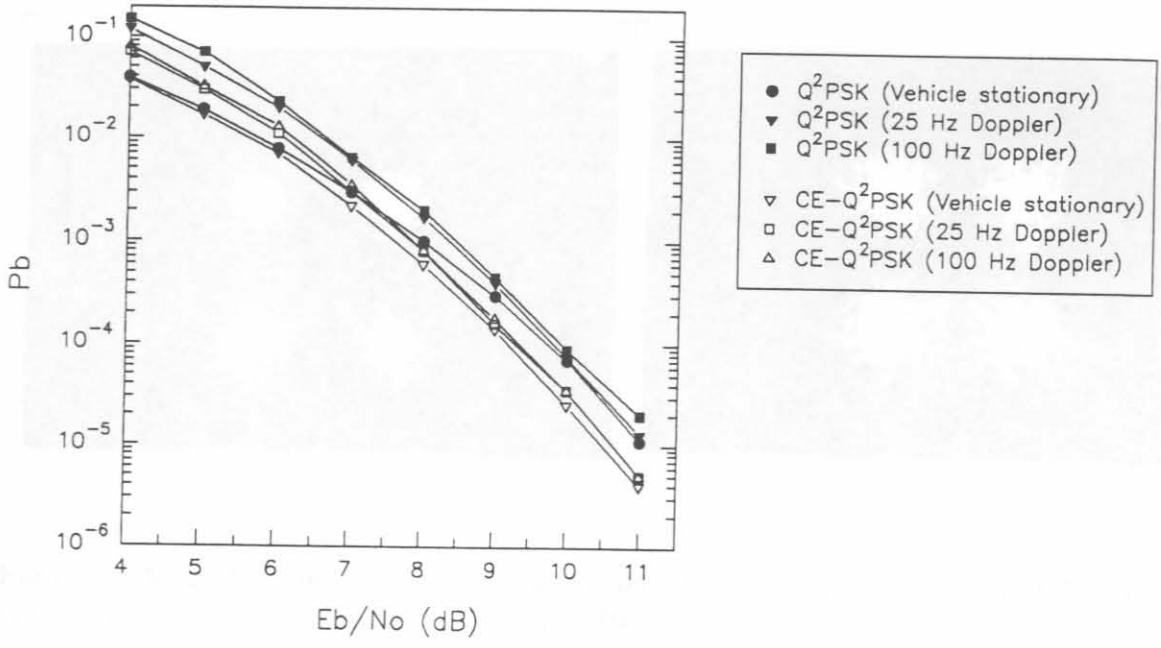

Figure 7.24: BEP curves for Q²PSK and CE-Q²PSK with DPFKE activated.

7.2.3 DSP implementation

The TMS320C30 floating point Digital Signal Processing (DSP) chip from Texas Instruments, provides an ideal platform for the suitable implementation of modems [89, 90, 91]. The DSP is fully programmable in *C* or in *assembler*.

For the implementation of the Q²PSK modulator and demodulator on the DSP, all the frequencies and sampling instants were scaled down by a factor of 10. This is done to eliminate the necessity to optimize the *C30* source code for true "real time" operation, because the aim of the exercise was only to verify the modulator and demodulator implementation principles. When the simulation code is optimized, or directly written in assembler and then cross-compiled to produce machine code, a speed-up factor of at least 10 times can easily be achieved.

Figures 7.25(a) and (b) depict the two 2D Q²PSK signal constellations associated with the cosine-carrier information (see Figure 4.7) under static AWGN channel conditions, for values E_b/N_o of 20.0 and 15.0 *dB*, respectively. Figures 7.26 to 7.27 similarly depict the two 2D Q²PSK signal constellations associated with the cosine-carrier information under mobile channel conditions at a RF

carrier frequency of 900 MHz. Specifically the constellation depicted by Figure 7.26(a) correspond to the cosine-carrier for a constant phase uncertainty θ_o of 0.1 *rad*, while Figure 7.26(b) corresponds to a Doppler frequency of 100.0 Hz, both for a E_b/N_o of 25.0 dB. Note that these figures correspond well to that obtained by computer simulation (refer to Figures 7.11 to 7.19). The constellations depicted in Figure 7.27 corresponds to the Q^{2}PSK signal space constellations associated with the cosine-carrier information (see Figure 7.27(a)) and cosine-sine-carrier information associated with shaping function $q_1(t)$ (see Figure 7.27(a)) for a constant phase offset $\theta_o = 0.1$ *rad*, a Doppler frequency $f_D = 50.0$ Hz and $E_b/N_o = 15.0$ dB.

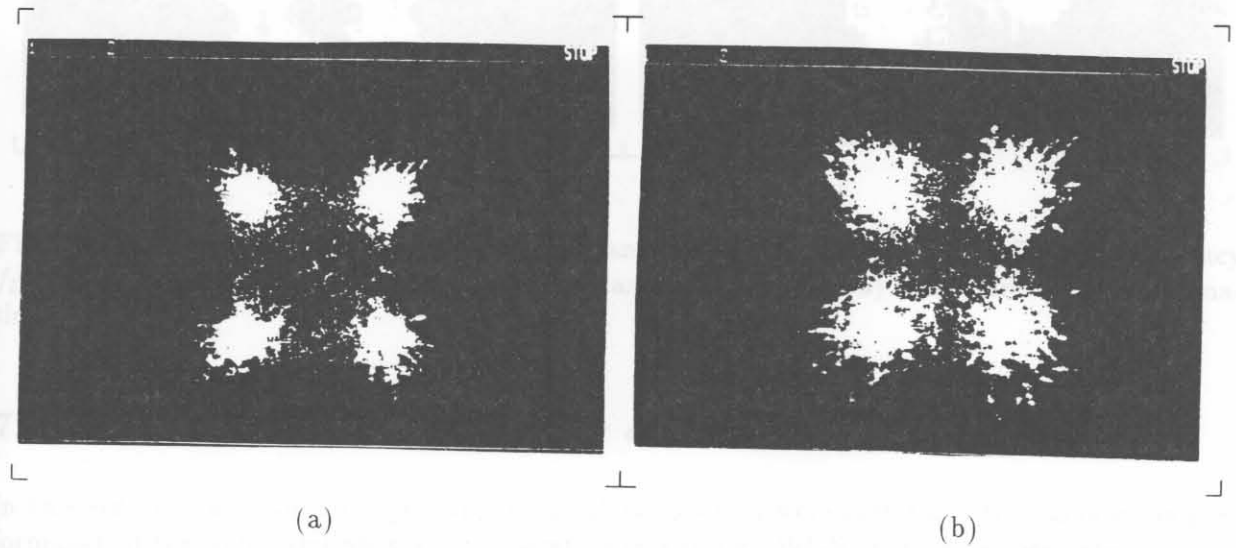

(a) (b)

Figure 7.25: Q^{2}PSK constellations (cosine-carrier information) under static AWGN channel conditions (a) $E_b/N_o = 20.0$ dB (b) $E_b/N_o = 15.0dB$.

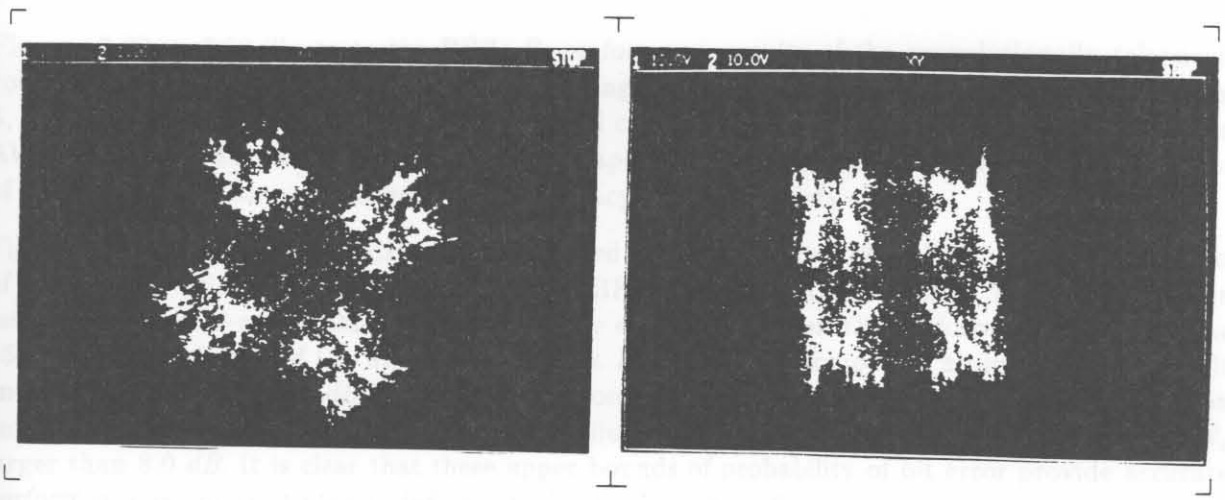

(a) (b)

Figure 7.26: Q^{2}PSK constellations (cosine-carrier information) under mobile channel impairments for $E_b/N_o = 25$ dB (a) carrier phase offset $\theta_o = 0.1$ *rad* (b) Doppler frequency $f_D = 100.0$ Hz.

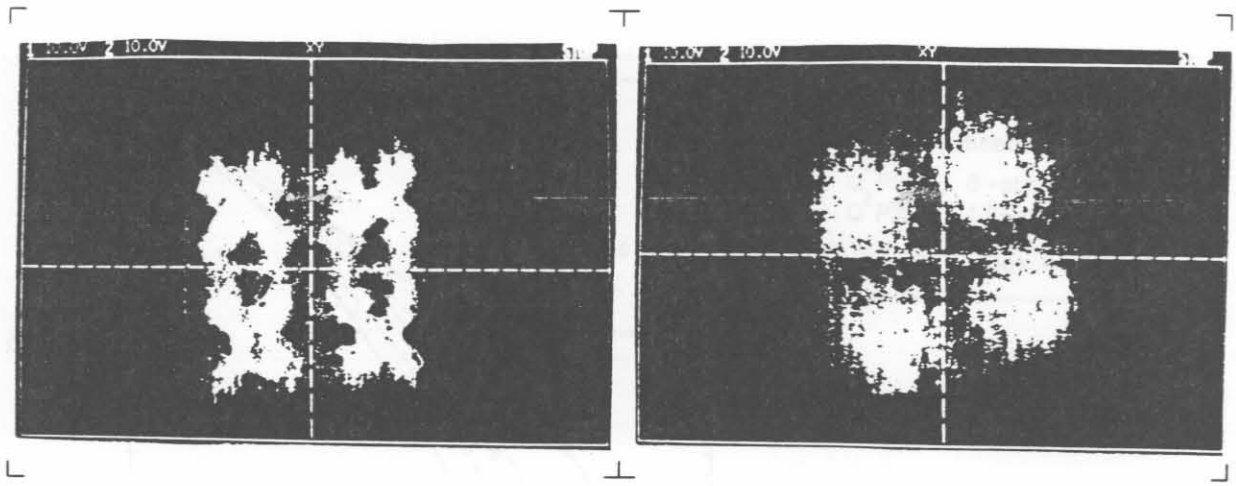

(a) (b)

Figure 7.27: Q²PSK constellations for a constant phase offset $\theta_o = 0.1$ *rad*, a Doppler frequency $f_D = 50.0$ *Hz* and $E_b/N_o = 15.0$ *dB* (a) cosine-carrier information (b) cosine-sine-carrier information.

7.2.4 Classical and TCM error correction in AWGN

In this section, the results of the software simulations which were performed to evaluate the performance of the coded Q²PSK systems operating in a static AWGN channel are presented. For all the simulation tests, perfect carrier and time synchronisation were assumed.

7.2.4.1 Classical error correction

Figures 7.28 to 7.30 illustrate the BER, P_b performance results of the convolutionally (classical) coded Q²PSK and CE-Q²PSK systems. Employing the Union bound approach described in Chapter 5, the performance of the different convolutional coded Q²PSK systems have been evaluated in an AWGN channel. These results, presented in Chapter 5 are repeated in the BEP results as a means of comparison in order to benchmark the accuracy of these bounds.

Figure 7.28 illustrates the BEP results obtained for coded rate 1/2 Q²PSK, compared to that of uncoded Q²PSK and the upper bounds to BEP presented in Figure 5.7. For the simulation tests two 8-and 16-state rate-1/2 encoders were employed. When the performance curves of the 16-state coder to that of the uncoded system at $P_b = 10^{-5}$ are compared, an improvement in bit energy requirement of 2.0 *dB* is seen. Furthermore, it is noted from the figure that the simulation curves correspond well to the derived bounds (illustrated by the dashed lines) for values of E_b/N_o larger than 8.0 *dB*. It is clear that these upper bounds of probability of bit error provide accurate performance estimates to the coded system for $E_b/N_o > 8.0$ *dB*.

Figure 7.29 illustrates the BER performance results obtained for coded hybrid rate 1/2 constant envelope CE-Q²PSK, compared to that of uncoded CE-Q²PSK. As was the case for Q²PSK, the simulation tests were performed employing 8- and 16-state coders, the only difference being that a single rate-2/3 convolutional coder, together with the block coder to force a constant envelope, was employed (see Figures 5.3 and 5.6).

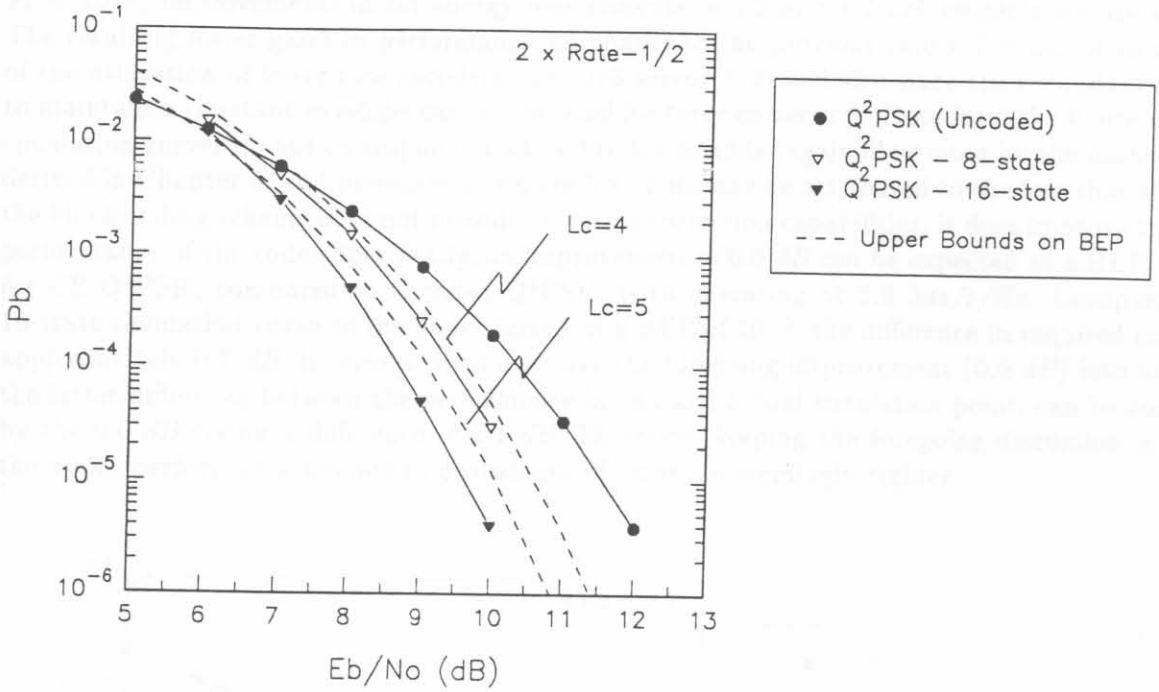

Figure 7.28: BEP graphs 8- and 16-state rate-2/4 Q^2PSK, compared to uncoded Q^2PSK and the upper bounds to BEP.

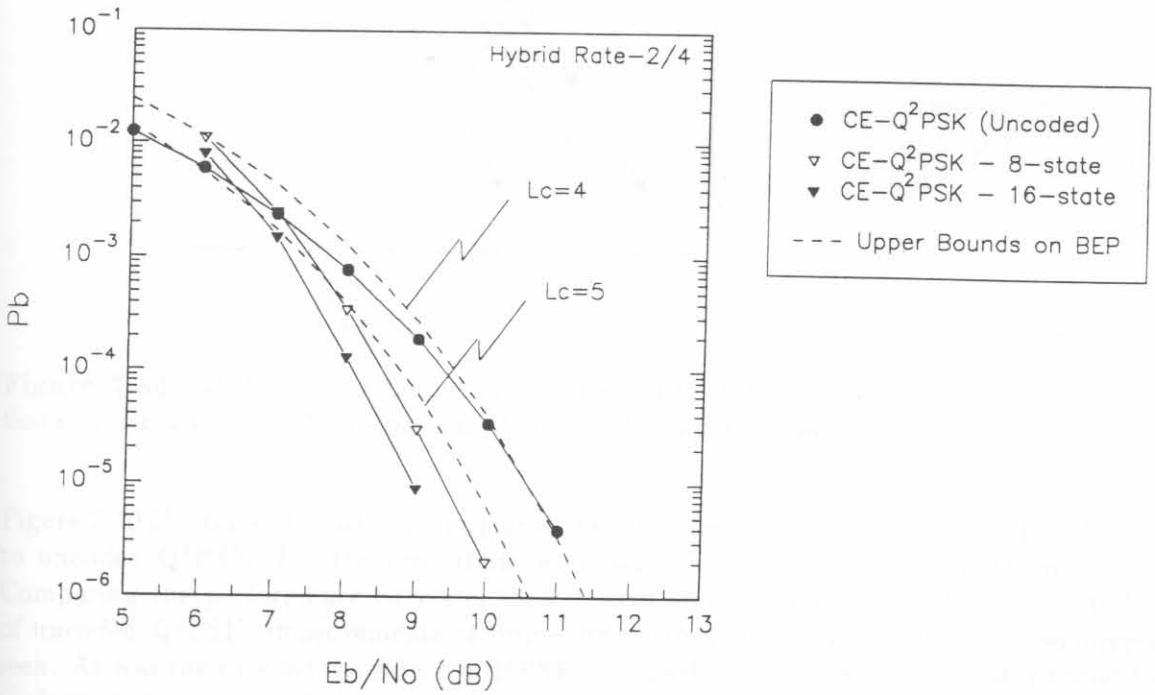

Figure 7.29: BEP graphs 8- and 16-state hybrid rate-2/4 Q^2PSK employing a single rate-2/3 convolutional coder, compared to uncoded CE-Q^2PSK and the upper bounds to BEP.

Comparing the performance curves of the 8- and 16-state coders to that of the uncoded system at $P_b = 10^{-5}$, improvements in bit energy requirements of 1.2 and 1.7 *dB*, respectively are evident. The resulting lower gains in performance, compared to the previous rate-1/2 coder, is as a result of the utilisation of lower rate encoders, (i.e. 2/3 versus 1/2) and also since the redundancy added to maintain a constant envelope can not be used for error correction. Note from the figure that the simulation curves do not correspond at all well to the bounds (again illustrated by the dashed lines) derived in Chapter 5, and presented in Figure 5.8. This may be attributed to the fact that although the block coding scheme does not provide any error correction capabilities, it does improve the noise performance of the code. Specifically, an improvement of 0.6 *dB* can be expected at a BEP of 10^{-5} for CE-Q^{2}PSK, compared to uncoded Q^{2}PSK, both operating at 2.0 *bits/s/Hz*. Comparing the 16-state simulation curve to the upper bound at a BEP of 10^{-5}, the difference in required energy is approximately 0.7 *dB*. However, when one take the foregoing improvement (0.6 *dB*) into account, the latter difference between the performance bound and actual simulation point, can be corrected by the 0.6 *dB* giving a difference of 0.1 *dB*. Therefore, keeping the foregoing discussion in mind, the upper performance bounds to probability of error are seemingly tighter.

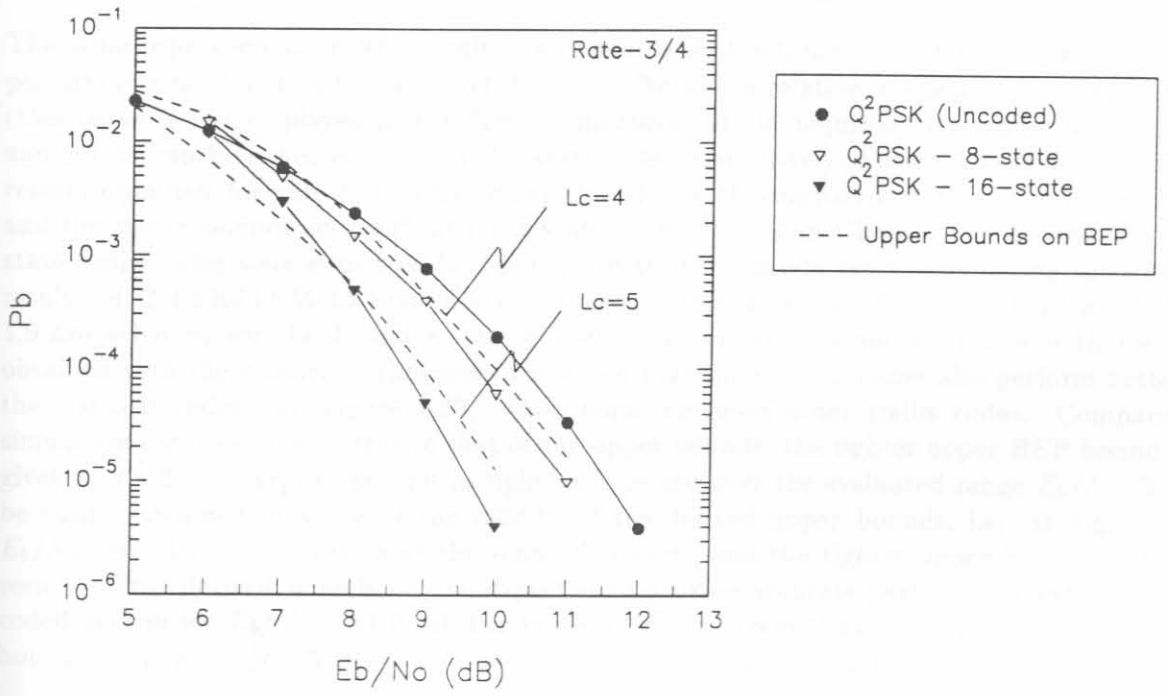

Figure 7.30: BEP graphs 8- and 16-state rate-3/4 Q^{2}PSK employing a single rate-3/4 convolutional coder, compared to uncoded Q^{2}PSK and the upper bounds to BEP.

Figure 7.30 illustrates the BER performance results obtained for coded rate-3/4 Q^{2}PSK, compared to uncoded Q^{2}PSK. For the simulation tests, 8-and 16-state rate-3/4 encoders were employed. Comparing the performance curves of these 8- and 16-state codes at a BEP, $P_b = 10^{-5}$ to that of uncoded Q^{2}PSK, improvements of respectively, 0.6 and 1.8 *dB* in bit energy requirement are seen. As was the case for the rate-2/4 Q^{2}PSK code performance (Figure 7.29), it is noted from the performance results that the simulation curves correspond well to the derived upper bounds (see Figure 5.9) for values of E_b/N_o larger than 8.0 *dB*.

From the BER graphs shown it is clear that reasonable coding gains can be achieved by employing

simple low-complexity sub-optimal encoding and decoding strategies for Q^{2}PSK and its constant envelope CE-Q^{2}PSK version. Recall that the effective coding gain, G_c, is the dB decrease in signal energy per bit-to-noise power density ratio (E_b/N_o) to maintain the same error performance as uncoded transmission.

7.2.4.2 Evaluation of TCM strategies

Simulation results of the trellis codes for Q^{2}PSK/TCM on the static AWGN channel are shown in Figures 7.31 to 7.32. Figure 7.31 illustrates the BEP results obtained for rate-2/4 trellis coded Q^{2}PSK/TCM and CE-Q^{2}PSK/TCM, compared to that of uncoded Q^{2}PSK. For the simulation tests 4-and 8-state trellis codes were evaluated. Comparing the performance curves at a BEP of $P_b = 10^{-5}$. Comparing the simulation results of Q^{2}PSK/TCM to that of the uncoded system, coding gains of 1.6 and 2.6 are achieved for the 4- and 8-state encoders, respectively. Comparing this with the results obtained with the classical techniques, it is noted that the trellis codes perform better than the classical codes (see Figure 7.28). Furthermore, these improvements are brought about with lower order trellis codes and therefore also lower complexity.

The same improvements in BEP results are evident when the trellis coded CE-Q^{2}PSK/TCM system performance is compared to the uncoded system. Note that relative to the uncoded Q^{2}PSK system (this curve is not displayed in the figure), improvements in required bit energy in excess of 1.3 and 2.5 dB can be expected, for 4- and 8-state codes, respectively. Figure 7.32 illustrates the BEP results obtained for rate-3/4 trellis coded Q^{2}PSK/TCM, compared to that of uncoded Q^{2}PSK and the upper bounds on BEP for the 8-state code (derived in Chapter 5). As before, 4-and 8-state trellis codes were evaluated for the performance simulation tests. Comparing the simulation results of Q^{2}PSK/TCM to that of the uncoded system at $P_b = 10^{-5}$, coding gains of 0.5 and 1.9 are achieved for the 4- and 8-state encoders, respectively. Comparing this with the results obtained with the classical techniques, it is noted that these trellis codes also perform better than the classical codes (see Figure 7.30), while requiring lower order trellis codes. Comparing the simulation curves of the 8-state to that of the upper bounds, the tighter upper BEP bound (UB2) given by (A.21) is surprisingly not as tight as expected over the evaluated range E_b/N_o. This can be easily explained in terms of the validity of the derived upper bounds, i.e. at high values of E_b/N_o. By close investigation of the simulation curve and the tighter upper bound (UB2), it is seen that the derived bounds can be expected to provide accurate performance estimates to the coded system for $E_b/N_o > 11.0$ dB. For values of E_b/N_o lower than 11.0 dB, the less tight upper bound, UB1 (given by (A.20) should be used as performance estimate.

7.3 EVALUATION ON FADING CHANNELS

We consider a typical mobile channel, which is both power-limited and bandwidth-limited. In a mobile channel the available bandwidth is constraint to accommodate a large number of users in a given transmission bandwidth, and power is constrained by the flux density limitation of the mobile (radio or satellite) transmitter's transmission and the physical size of the mobile's antenna. In addition to the usual additive thermal noise background, the mobile channel is also impaired by Doppler frequency shift due to vehicle motion, the potential of a nonlinear channel due to non-linear amplifiers in the transmitter, voice delay, multipath fading and shadowing. The latter two are most definitely the most serious, whereas for reliable performance the system must be able to be robust under short fades and recover quickly from long fades.

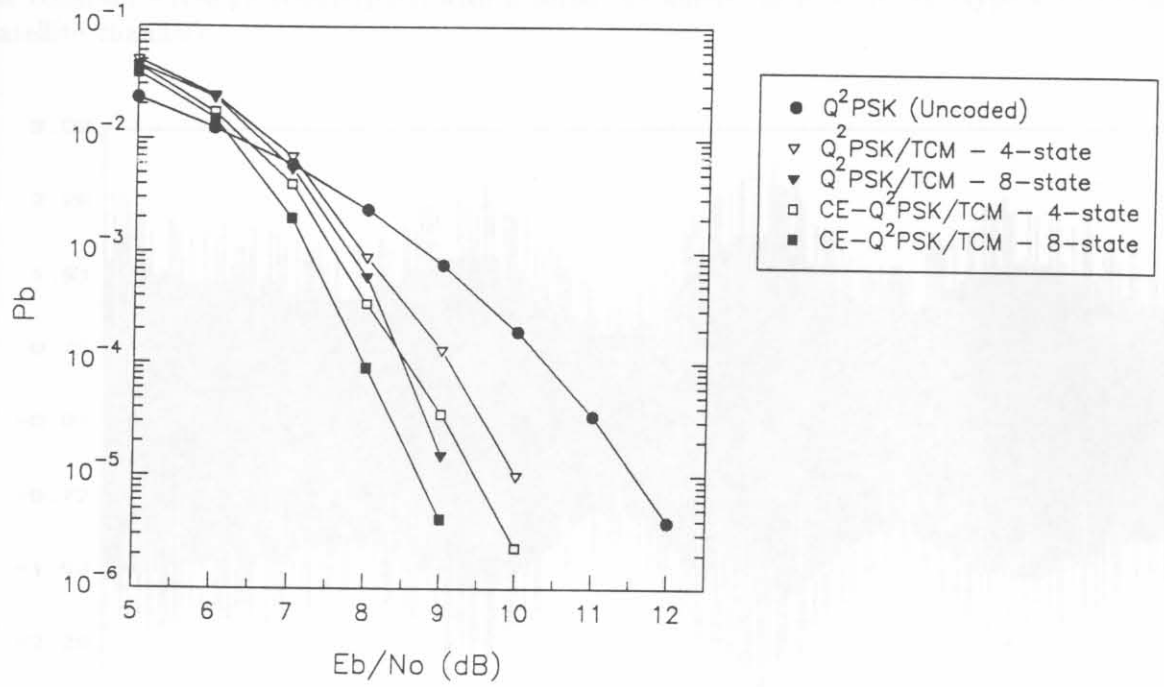

Figure 7.31: BEP graphs 8- and 16-state rate-2/4 Q^2PSK/TCM and CE-Q^2PSK/TCM compared to uncoded Q^2PSK.

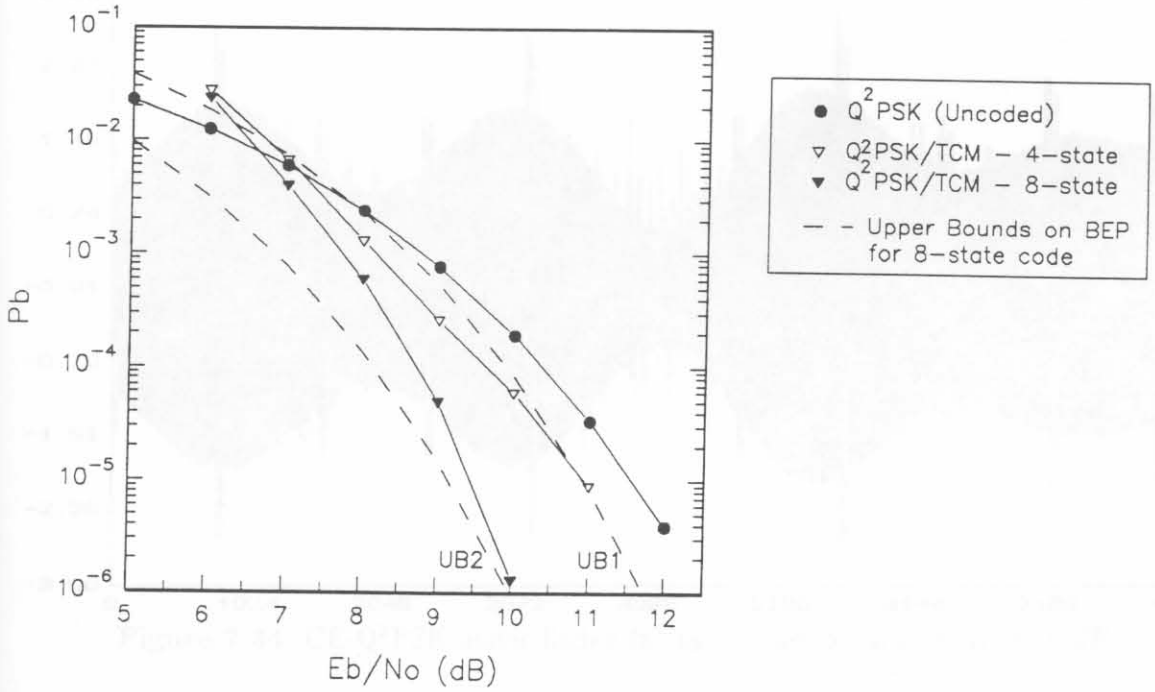

Figure 7.32: BEP graphs 8- and 16-state rate-3/4 Q^2PSK/TCM, compared to uncoded Q^2PSK.

Figures 7.33 and 7.34 depict the Rician faded discrete time (i.e., sampled) signals for Q^2PSK and its constant envelope counterpart, with a Rician parameter of $K = 10$ dB (typical of the mobile satellite channel).

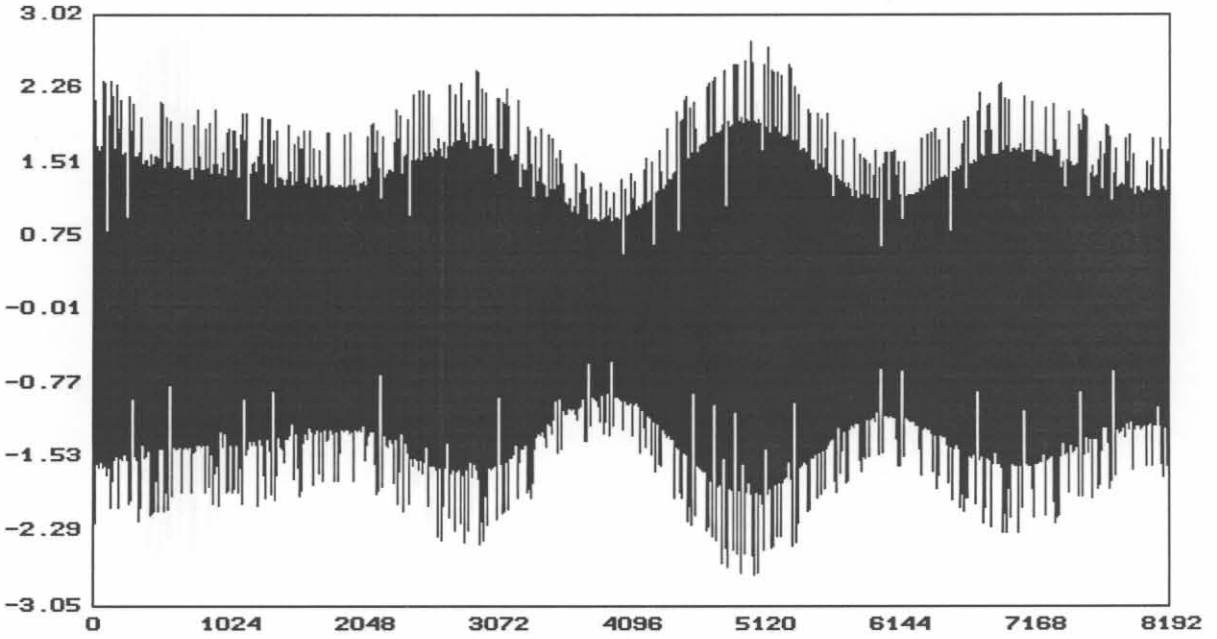

Figure 7.33: Q^2PSK under Rician fading channel conditions, $K = 10$ dB.

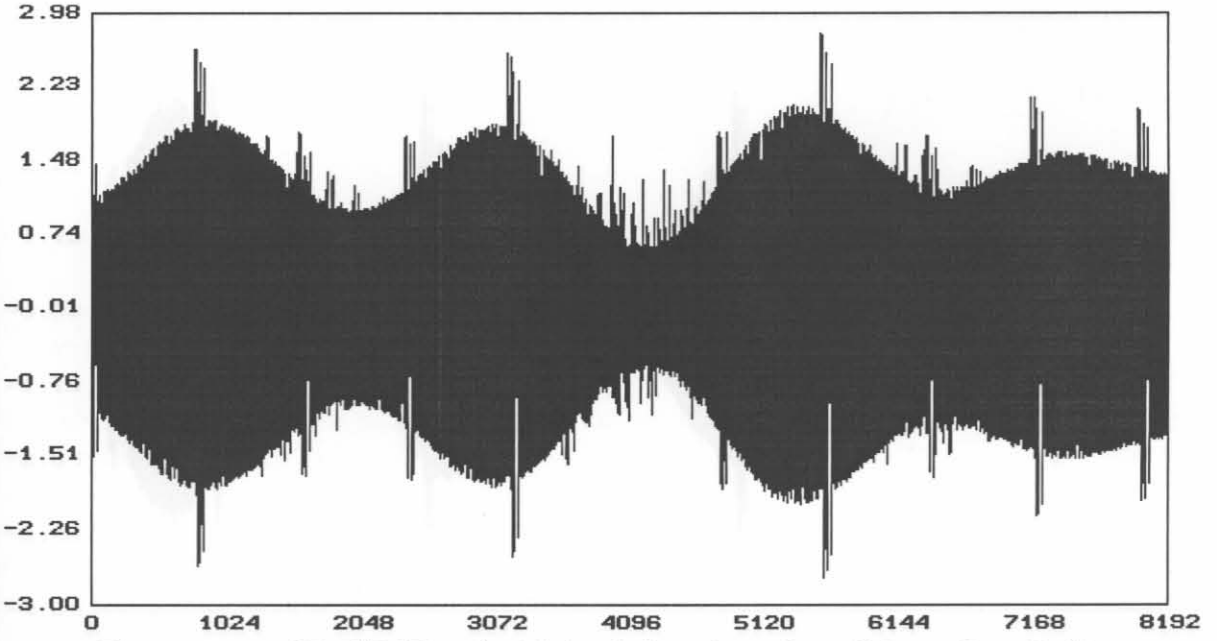

Figure 7.34: CE-Q^2PSK under Rician fading channel conditions, $K = 10$ dB.

Figures 7.35 and 7.36 depict the Rayleigh faded discrete time signals for Q^{2}PSK and CE-Q^{2}PSK, with a Rician parameter of $K = 0$ dB. For these channel conditions, the Line-of-Sight (LOS) (coherent) component is totally blocked out (typical of the land mobile channel).

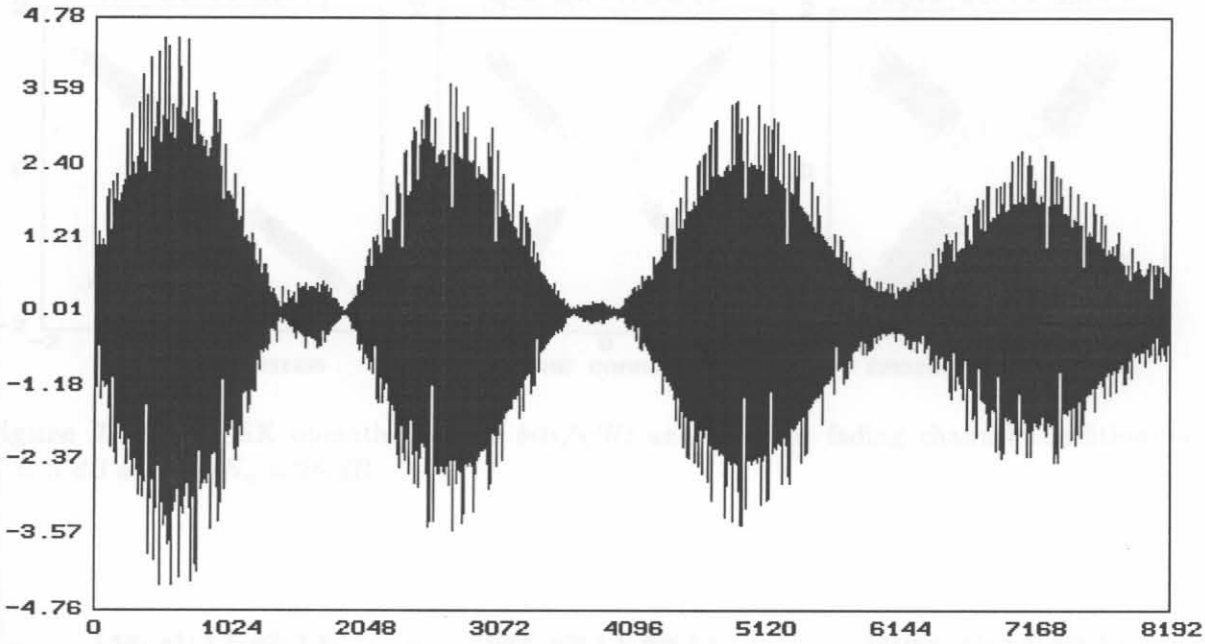

Figure 7.35: Q^{2}PSK under Rayleigh fading channel conditions, $K = 0$ dB.

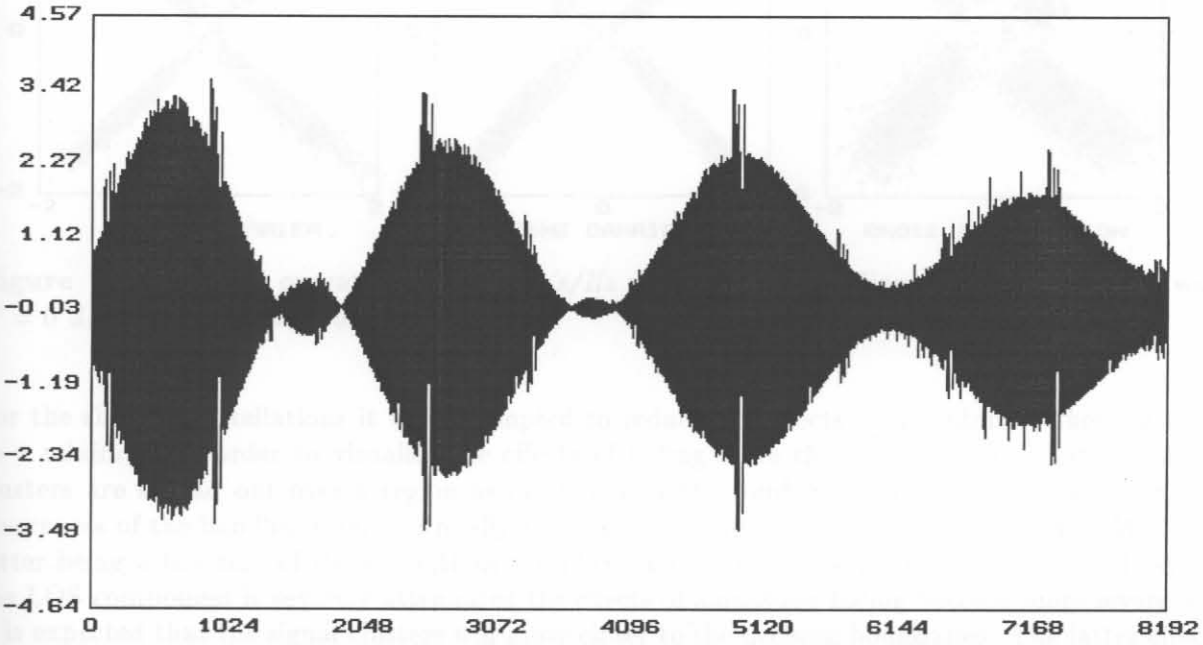

Figure 7.36: CE-Q^{2}PSK under Rayleigh fading channel conditions, $K = 0$ dB.

We again consider the signal space constellations as an effective way of displaying the detrimental effects of mobile fading channels. Figures 7.37 to 7.38 show the bandlimited Q^{2}PSK signal constel-

lations operating at 2.0 *bits/s/Hz* under typical mobile fading channel conditions in AWGN with $E_b/N_o = 25.0$.

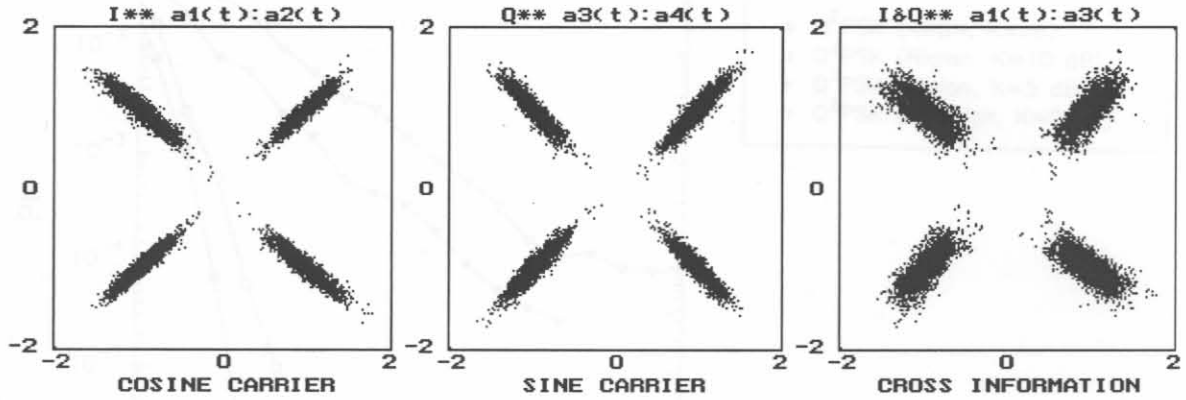

Figure 7.37: Q^{2}PSK operating at 2.0 *bits/s/Hz* under Rician fading channel conditions with $K = 5$ *dB* and $E_b/N_o = 25$ *dB*.

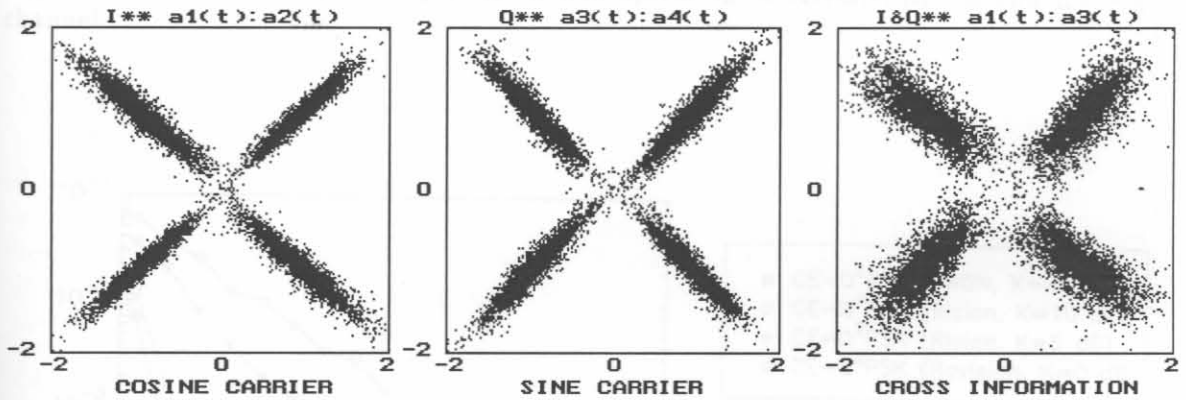

Figure 7.38: Q^{2}PSK operating at 2.0 *bits/s/Hz* under Rayleigh fading channel conditions with $K = 0$ *dB* and $E_b/N_o = 25$ *dB*.

For the shown constellations it was attempted to reduce the effects of the additive thermal noise to a minimum in order to visualise the effects of fading more clearly. It is seen that the signal clusters are spread out over a region associated with the combined effects of thermal noise, the severeness of the bandlimiting, and finally the effects of mobile channel amplitude fades. With the latter being a function of the strength of the LOS component in the fading channel model. When the LOS component is severely attenuated the effects of amplitude fading become more severe and it is expected that the signal clusters will move closer to the decision boundaries. The latter effects are clearly visible on the constellations depicted in Figure 7.38 where the LOS component power is taken to be equal to the power in the scatter components (i.e., dual equal amplitude propagation model [63]).

Figures 7.39 to 7.40 show the BER results of the Q^{2}PSK and CE-Q^{2}PSK modem operating at

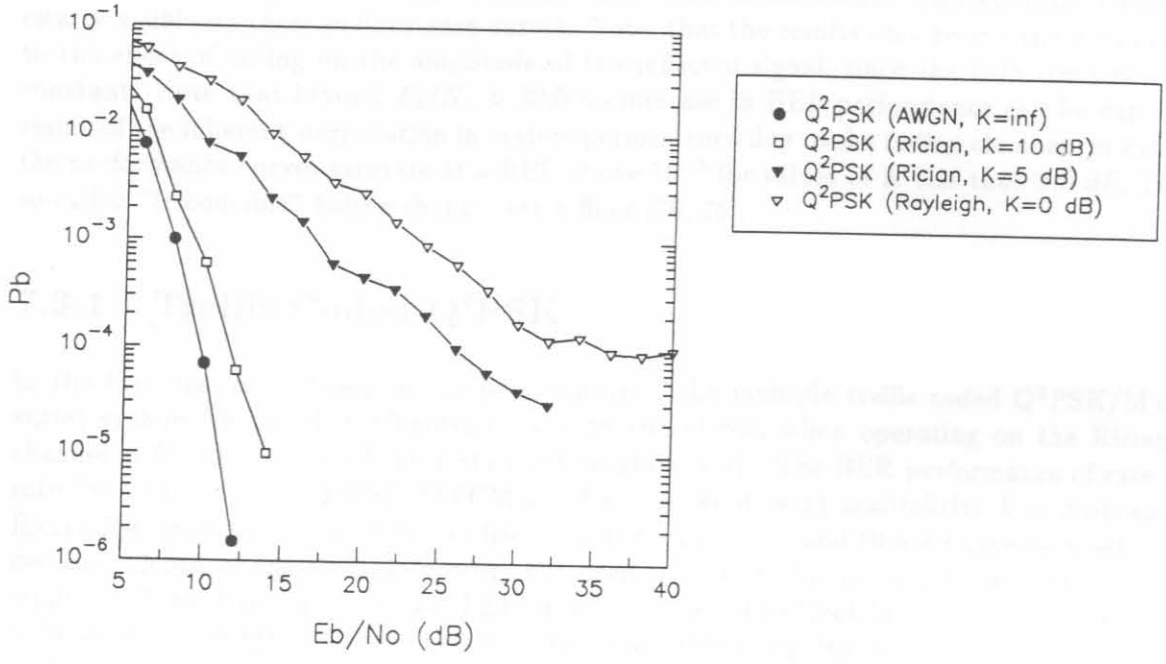

Figure 7.39: BER results for Q^2PSK modem operating on AWGN, Rician and Rayleigh fading channel.

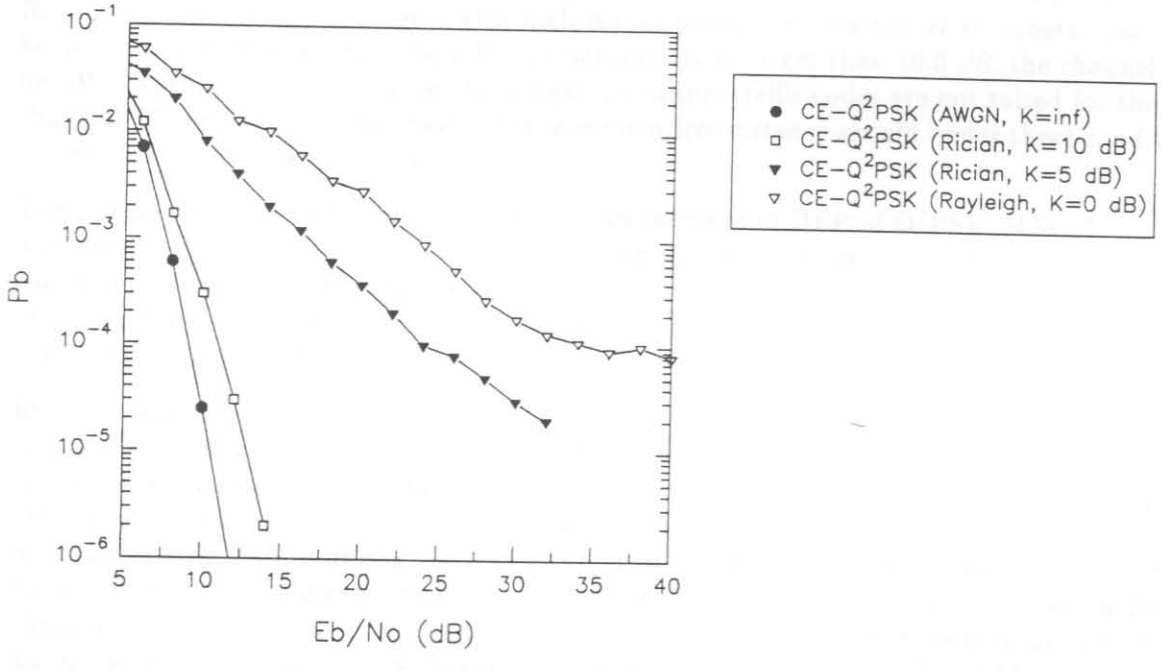

Figure 7.40: BER results for CE-Q^2PSK modem operating on AWGN, Rician and Rayleigh fading channel.

2.0 *bits/s/Hz*, under AWGN, Rician ($K = 5, 10$ *dB*), and Rayleigh ($K = 0$ *dB*) fading channel conditions. The degradation in performance as a result of the mobile channel fading conditions are clearly visible on these performance curves. Note, that the results only reflect the degradation due to the effect of fading on the amplitude of the reflected signal, since the LOS component is kept constant. Note that beyond $E_b/N_o > 30.0$ no increase in BEP performance can be expected as a result of the inherent degradation in system performance due to the fading channel. In other words the performance curves saturate at a BEP above 10^{-5} for values of K less than 5.0 *dB*. This is the so-called "irreducible" fading channel error floor [76, 75].

7.3.1 Trellis Coded Q^{2}PSK

In the first part of this section the performance of the multiple trellis coded Q^{2}PSK/MTCM (4-state) system (designed in Chapter 6) will be considered, when operating on the Rician fading channel in the absence of Channel State Information (CSI). The BER performance of rate-6/8 and rate-5/8 coded 4-state Q^{2}PSK/MTCM will be considered, with multiplicity $k = 2$ obtained on a Rician fading channel. Two different Rician factors of $K = 5.0$ and 10.0 *dB* have been selected. The decoding depth of the Viterbi decoders has been selected to be at least 4 times the length of the minimum Error Event Probability (EEP) in all the cases. The block bit interleaving size was chosen to be equal to 196 Q^{2}PSK coded symbols, with the interleaving depth equal to 16 symbols (64 bits), and the interleaver span equal to 12 symbols (48 bits). This will cause a worst case-delay (due to the block interleaver) of 768 coded Q^{2}PSK information bits. When one considers a transmission rate of $R_b = 20.0$ *kbits/s*, the worst case-delay will be 38.4 *ms*, which is quite acceptable for the transmission of digitally encoded speech [58, 76].

Results of the Rician fading channel for $K = 10$ *dB* are shown in Figure 7.41. The important point made in this figure is that the improvement in achievable BEP performance for MTCM codes under Rician channel fading conditions, with high Rician parameter, are not at all substantial. This can be attributed to the fact that for a Rician parameter, K larger than 10.0 *dB*, the channel tends to be AWGN, that is the criteria for the design of multiple trellis codes are not suited for these fading channels. Therefore, maximisation of the minimum free distance should under these conditions still be the primary design objective.

The foregoing is clear when we consider the improvement in BEP of Q^{2}PSK/MTCM compared to uncoded Q^{2}PSK, operating on the Rician fading channel with $K = 5$ *dB*. Importantly, we note that the probability of error for the rate-6/8 and 5/8 codes varies inversely with $(E_s/N_o)^2$, because of the length of the shortest EEP (or code diversity) is equal to 2. Note that when the multiplicity is increased to $k = 4$, the probability of error is expected to vary inversely with $(E_s/N_o)^4$.

In the foregoing discussion no CSI was available during the demodulation process. Recall, that the metric chosen for the Viterbi decoder depends on whether or not CSI can be obtained. As discussed in Chapter 3 (see Figure 3.3), a measure of CSI can be obtained from the channel state extractor. For our application, the use of the magnitudes of the complex correlation function at the optimum timing instant during the frame and symbol synchronisation period, has been considered to determine the fading magnitude over the header interval, This is used as a direct indication of channel state or reliability. In general, any other measure could have been employed. Consider, for instance the utilisation of a channel estimator based on a recursive Least Mean Square (LMS) estimator. The latter technique was found to be as effective as the correlation-magnitude method, but at a much higher complexity.

Employing the correlation-magnitude as an indication of CSI, i.e., the reliability or state of the

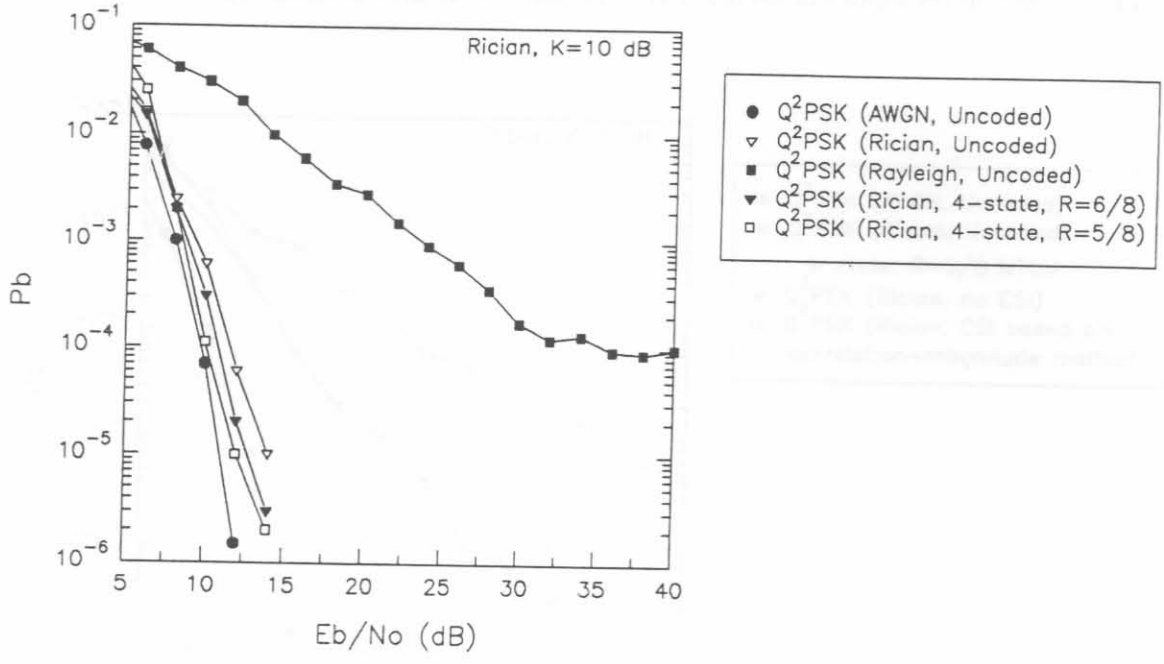

Figure 7.41: BER results for 4-state rate-6/8 and rate-5/8 Q²PSK/MTCM operating on Rician ($K = 10$ dB) fading channel.

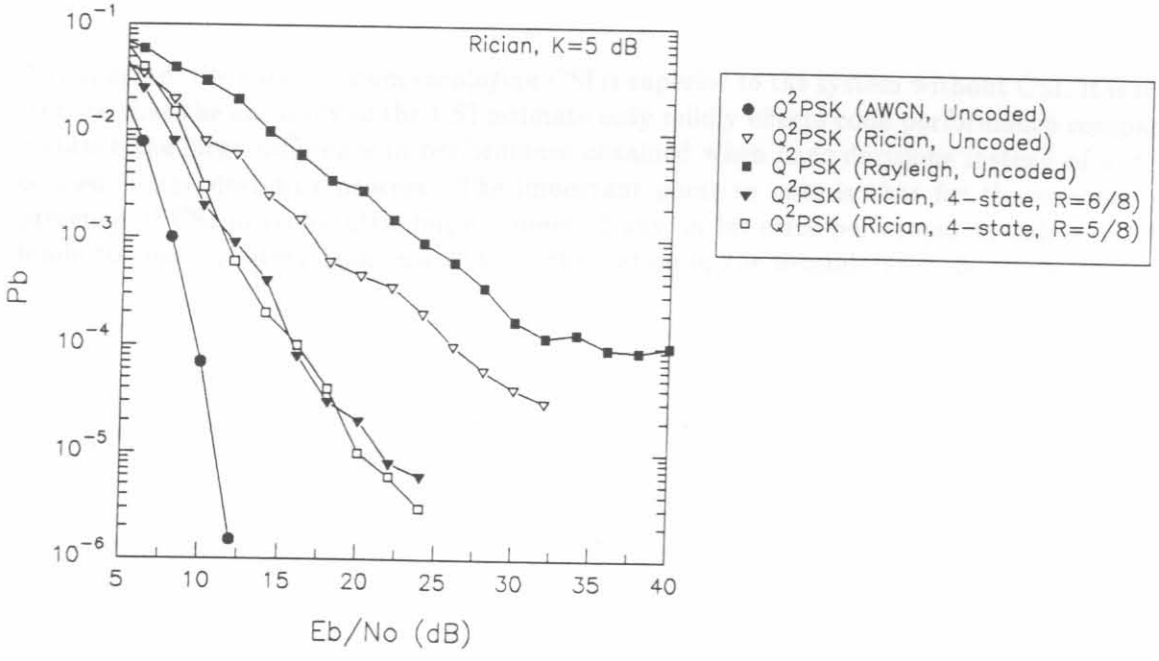

Figure 7.42: BER results for 4-state rate-6/8 and rate-5/8 Q²PSK/MTCM modem operating on Rician ($K = 5$ dB) fading channel.

channel, the performance of the 4-state rate-5/8 Q^2PSK/MTCM coded system was evaluated on the Rician fading channel, with $K = 5$ dB. The BEP curves are depicted in Figure 7.43.

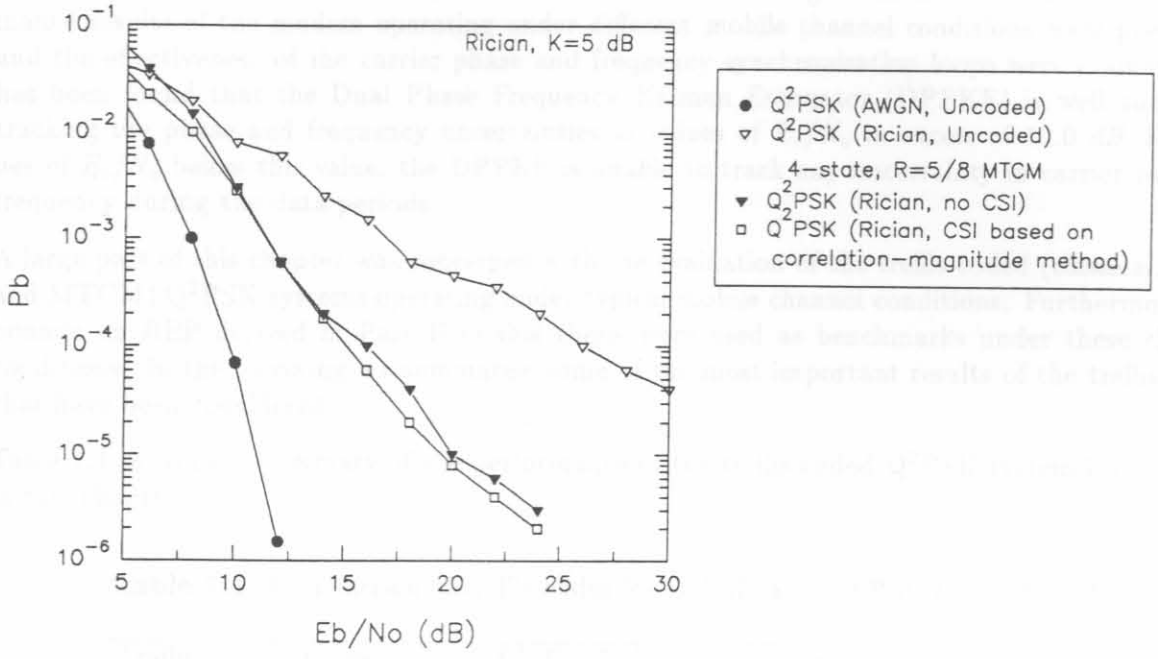

Figure 7.43: BER results for 4-state rate-5/8 Q^2PSK/MTCM modem operating on Rician ($K = 5$ dB) fading channel without and with CSI based on the correlation-magnitude of the frame and symbol synchronisation process.

As expected, the coded system employing CSI is superior to the system without CSI. It is interesting to note that the accuracy of the CSI estimate only mildly effects code performance compared to for instance the large difference in performance obtained when hard decisions instead of soft decisions is used in the decoding process. The important point to note is that for the uncoded case, the presence of CSI provides little improvement, if any, in bit error performance, unless an attempt is made to constructively make use of this information in the demodulator/detection process.

7.4 CONCLUDING REMARKS: CHAPTER 7

In this chapter an extensive simulation performance evaluation of the Q²PSK and CE-Q²PSK modems have been carried out under AWGN and mobile fading channel conditions. The performance results of the modem operating under different mobile channel conditions were presented, and the effectiveness of the carrier phase and frequency synchronisation loops were evaluated. It has been found that the Dual Phase Frequency Kalman Estimator (DPFKE) is well suited for tracking the phase and frequency uncertainties at values of E_b/N_o in excess of 10.0 *dB*. For values of E_b/N_o below this value, the DPFKE is unable to track any uncertainty in carrier phase or frequency during the data periods.

A large part of this chapter was concerned with the evaluation of the trellis coded (classical, TCM and MTCM) Q²PSK systems operating under typical mobile channel conditions. Furthermore, the bounds on BEP derived in Part II of this thesis were used as benchmarks under these channel conditions. In the following we summarise some of the most important results of the trellis codes that have been considered.

Table 7.1 provides a summary of the performance of the trellis coded Q²PSK system investigated in this chapter.

Table 7.1: Comparison of trellis codes for Q²PSK at a BEP of $P_e = 10^{-5}$ *dB*.

Trellis Code	Code Rate, R_c	No. of states	E_b/N_o for $P_e \leq 10^{-5}$	Channel	Gain, G_c over uncoded Q²PSK
Classical	2/4	8	10.3 *dB*	AWGN	1.1 *dB*
Classical	2/4	16	9.4 *dB*	AWGN	2.0 *dB*
Classical	2/4(*CE*)	8	9.6 *dB*	AWGN	1.8 *dB*
Classical	2/4	16	9.0 *dB*	AWGN	2.4 *dB*
Classical	3/4	8	10.9 *dB*	AWGN	0.5 *dB*
Classical	3/4 (CE)	16	9.7 *dB*	AWGN	1.7 *dB*
TCM	2/4	4	10.0 *dB*	AWGN	1.4 *dB*
TCM	2/4	8	9.0 *dB*	AWGN	2.4 *dB*
TCM	2/4 (CE)	4	9.6 *dB*	AWGN	1.8 *dB*
TCM	2/4 (CE)	8	8.7 *dB*	AWGN	2.7 *dB*
TCM	3/4 (CE)	4	11.0 *dB*	AWGN	0.4 *dB*
TCM	3/4 (CE)	8	9.6 *dB*	AWGN	1.8 *dB*
MTCM	6/8	4	13.0 *dB*	Rician ($K = 10$)	1.5 *dB*
MTCM	5/8	4	12.0 *dB*	Rician ($K = 10$)	2.5 *dB*
MTCM	6/8	4	22.0 *dB*	Rician ($K = 5$)	> 13.0 *dB*
MTCM	5/8	4	20.0 *dB*	Rician ($K = 5$)	> 15.0 *dB*
MTCM (CSI)	5/8	4	17.5 *dB*	Rician ($K = 5$)	> 17.5 *dB*

The performance is compared to the corresponding performance of uncoded Q²PSK, expressed as a coding gain, G_c in *dB*. From the table it can be seen that the low rate classical convolutional codes provided good performance, compared to their relative complexity. The hybrid rate-2/4 code, employing the single rate-2/3 convolutional encoder, provides the best performance of all the classical error correction strategies considered. This is in spite of the lower expected performance of

the rate-2/3 encoder, when compared to that of the rate-1/2 encoders of the non-constant envelope Q^2PSK system. It should therefore be clear that the choice of constant envelope coded scheme should be strongly considered for application on non-linear channels.

When we compare the performance of the trellis coded modulation codes, similar observations are made. Specifically, the performance of the rate-2/4 trellis coded constant envelope Q^2PSK provides the best performance under AWGN channel conditions. The rate-3/4 trellis codes also provide relatively high coding gains, compared to that of the uncoded Q^2PSK system, without a substantial reduction in throughput rate.

Finally, we compare the multiple-trellis codes, specifically designed for transmission over the fading channel, with and without the availability of CSI.

In the first part of this section the performance of the multiple trellis coded Q^2PSK/MTCM (4-state) system operating on the Rician fading channel in the absence of Channel State Information (CSI) was considered. For all the simulation results a block interleaver was employed with bit interleaving size was chosen to be equal to $16 \times 12 = 196$ Q^2PSK coded symbols. We have considered the bit error rate performance of rate-6/8 and rate-5/8 coded 4-state Q^2PSK/MTCM, with multiplicity $k = 2$ obtained on a Rician fading channel for two different Rician factors of 5.0 and 10.0 *dB*.

From the results of the Rician fading channel for $K = 10$ *dB*, shown in Figure 7.41, it can be seen that the coding gains achieved by the 4-state MTCM are not as high as one may have expected. The important point to keep in mind when considering these results, is that the trellis codes which are optimum for the AWGN channel, will also be optimum for the Rician channel, when K is greater than 5.0 *dB*. This can be attributed to the fact that a Rician channel, K larger than 5.0 *dB* strongly resembles an AWGN channel.

Comparing the results of the 4-state Q^2PSK/MTCM, at the same code rates operating on the Rician fading channel for $K = 5$ *dB*, a large increase in coding gains is noted. Recall, that for a code multiplicity $k = 2$, the probability of error of the 4-state rate-6/8 and 5/8 codes varies inversely with $(E_s/N_o)^2$, since the length of the shortest EEP is equal to $k = 2$.

Therefore, it is concluded that some of the optimum codes specially designed for the AWGN channel, may also be very suitable for application over fading channels with Rician parameter in excess of 5.0 *dB*. This is true, since in channels with K large, the diversity factor does not significantly influence the BEP behavior of the codes.